DYNAMIC CHARACTERIZATION OF A MICRO HEAT ENGINE

By

HAMZEH KHALID BARDAWEEL

A thesis submitted in partial fulfillment of
the requirements for the degree of

MASTER OF SCIENCE IN MECHANICAL ENGINEERING

WASHINGTON STATE UNIVERSITY
School of Mechanical and Materials Engineering

December 2007

To the Faculty of Washington State University:

The members of the Committee appointed to examine the thesis of HAMZEH KHALID BARDAWEEL find it satisfactory and recommend that it be accepted.

_____
Chair

_____

_____

ACKNOWLEDGMENT

Foremost, I would like to thank my adviser Dr.Cill Richards for her support and guidance over the last two years. I would like to thank Dr. Michael Anderson for developing the mathematical model and for his guidance and support through this work. Dr. Robert Richards requires special acknowledgment for his advice through my graduate work. Direct acknowledgment is required for Leland Weiss for the consistent help and support he offered me, and for Amer Hamdan for helping me editing my thesis text.

DYNAMIC CHARACTERIZATION OF A MICRO HEAT ENGINE

Abstract

by Hamzeh Khalid Bardaweel, M.S.
Washington State University
December 2007

Chair: Cill D. Richards

Micro heat engines have been proposed by different researchers to be used in the growing MEMS field. Such energy conversion devices are complex systems. Understanding the behavior of these devices is crucial to predict the optimization of the device parameters for the best performance. A complete mathematical model has been developed to capture the dynamic behavior of a micro heat engine, thus predicting the forces and displacements produced by addition of the heat to the engine. Newton's second law, conservation of energy, and mass and heat transfer equations are used to develop the model. The model has been validated against two engines, the "cantilever engine", and the "enclosed engine". In comparing the model prediction to the measured data the least squares method was used to estimate the unknown free parameters in the model. A favorable agreement between model prediction and experimental measurements is observed in both engines.

The results of the cantilever engine, in practice an actuator, showed that the displacement of the cantilever is maximized for low frequency operation. A resonant peak in the displacement occurred at f_p=200.0 Hz. Moreover, the results showed that the heat loss coefficient U, was most strongly correlated to bubble diameter. An engine with smaller bubbles experienced higher heat loss. The thermal inertia C_T was also correlated

with bubble size. An engine with bigger bubbles showed higher thermal inertia C_T. However, the vaporization coefficient β did not correlate with bubble size or cavity thickness. In addition to the displacement measurements, the voltage across the cantilever terminals was measured at different load resistances R_L, and then used to estimate the thermal to electric efficiency at those load resistances.

The results of the enclosed engine showed a linear behavior over a wide range of frequencies, up to 100 Hz. However, a departure from linearity started to appear at higher frequencies as the input energy to the engine increased.

The parameters, found to minimize the squares of the error between the model prediction and the measured data were the vaporization coefficient β =0.0003, frictional damping b_f=1.25 N.s/m, and heat loss coefficient U=0.0352 kJ/kg.K. Since the measured data showed no resonant peak in displacement up to 2.0 kHz , the effective mass of the engine was set $m + \bar{m} = 0$. The effect of the heat pulse duration T on the engine performance was examined. The results showed that, the amplitude of the velocity components U_k was maximized for the shorter heat pulse. Moreover, the amplitude of the velocity components U_k declined rapidly as frequency increased for the longer heat pulse duration. A short pulse duration is desirable, because the heat rate amplitudes Q_k have larger values over a wider frequency spectrum.

TABLE OF CONTENTS

CHAPTER 1

LITERATURE REVIEW

The need for micro-power sources to be used in the rapidly growing micro-electromechanical systems (MEMS) technology has led to the development of a micro-scale combustion engine field. This includes internal and external combustion heat engines, fuel cells, and microbatteries. In this work, two external combustion engines are presented. The first one is called a "cantilever engine" where the mechanical work is done on a PZT cantilever. This device is most suited to actuator applications. The other one is called an"enclosed micro heat engine" where the mechanical work is done on 2 μm thick silicon nitride membrane.

In the following sections, a literature review is presented. The review will focus on different methods of actuation as well as heat engines.

1.1 Actuation Mechanisms

Recently, there has been much interest in developing actuation mechanisms that can be fabricated reproducibly and can deliver relatively large displacements and forces [1]. Micro-actuators are used as the driving forces for different microsystems including microvalves, micropumps, and grippers. Different materials and actuation mechanisms have been proposed in development of micro-actuators [15]. Each actuation mechanism has its own advantages and disadvantages, in terms of displacement, forces, operating speed, dynamic response and performance stability.

In the literature different kinds of actuators are found: electrically driven actuators, including electromagnetic [2], electrostatic [3], and piezoelectric [4]. Thermally driven

actuators includes, thermal bimorphs [5], thermo- pneumatic [6] , and phase change actuators [7]. Each actuation mechanism is constrained by specific advantages and disadvantages.

1.1.1 Electrically Driven Actuators

A magnetic field can be used to produce force, torque or displacement of a microstructure. This phenomenon has been used as an actuation mechanism. In reference [2], integrated permanent magnet microactuators have been fabricated using micromachined polymer magnets. The magnets had the shape of thin disks with 4 mm diameter and 90 μm thicknesses. The disks were magnetized in the thickness direction. A cantilever beam-type magnetic actuator carrying the magnet disks on their free ends was fabricated on an epoxy board. A planar coil on the opposite side of the substrate was then used to drive the beams vertically. A driving current of 100mA used to generate a magnetic field. The maximum deflection of the beam was 15 μm. The difficulty to form on-chip, high efficiency solenoids [8] , in addition to the large driving currents required compared to other electrically driven actuators, are the main drawback of this technology [2].

The idea behind electrostatic actuation is that an electrostatic force develops between two conductors if a voltage is applied between them. Electrostatically driven micromotors were one of the earliest MEMS actuators [9]. A group at the university of Tokyo [10] constructed a large stepwise motion electrostatic actuator for a wireless microrobot application. Simulations showed that up to 240 nm displacements in the x-direction are achievable. Remote actuation of an array of actuators supporting 0.25 mm^2 and 380 μm

thick pieces of silicon was successfully demonstrated with an 80 V pull-in voltage. The main advantage of electrostatic actuators is their fast dynamic response [2]. However, the high voltage required for static actuators operation is considered a drawback. A high voltage introduces electronic complexity and material compatibility issues [8]. Also, they are difficult to adapt with many microvalve applications. Electrostatic actuators are environmentally sensitive for moisture and particulates and they require narrow gaps for large forces [1].

The ability of some materials to deform when an electric field is applied on it is known as the inverse effect of piezoelectricity. This phenomenon has been implemented as actuation mechanism. The *Alps* Corporation developed a small linear motor system using multilayered piezoelectric actuators, producing 3.6 N sliding force [11]. Friend *et al* [12] developed a linear piezoelectric actuator with a maximum force 1.86 N. A linear piezoelectric actuator using a cantilever bimorphs was constructed [13]. The cantilever was vibrated in both the fundamental axial mode and high order flexural mode. The force and the sliding velocity achieved were 0.09N and 27.7 cm/s respectively. An approximate efficiency of 1% was obtained from an actuator composed of four closely- matched bimorphs. A major drawback of common piezoelectrics is that they contain lead which is not compatible with the complementary metal oxide semiconductor(CMOS) process. Also, piezoelectric actuators provide relatively small displacements when solid stacks are used and small forces when bimorphs are used[1].

1.1.2 Thermally Driven Actuators

Actuation of a microscale devices can be achieved by adding and removing heat. A change in the temperature profile of a microstructure results in displacement or force

output. Adding heat to a microstructure can be achieved by ohmic heating, conduction, convection and absorption of electromagnetic waves. Cooling the microstructure can be achieved by conduction, convection and radiation dissipation [14].

As a thermal actuation method, a thermal bimorph actuator consists of two materials joined together along their longitudinal axis. Upon heating, the structure bends with different thermal coefficients of expansion to produce a displacement. A thermal vertical bimorph actuator fabricated of silicon beams side-coated with aluminum was constructed [8]. The fabricated device was 600 μm in length and the thicknesses of the silicon and aluminum layers were 4.2 μm, and 3.1 μm respectively. An input power to the actuator of 3.2 mW resulted in 4.8 μm deflection. The time constant was measured to be 0.5 ms. The main disadvantages of the thermal bimorph actuators are the slow response, large power consumption and sensitivity to environmental temperature changes.

Another kind of thermal actuation is thermo-pneumatic actuation. A thermo-pneumatic actuator consists of a sealed cavity filled with fluid, usually fluorinert liquid, and a flexible diaphragm on the boundary of the cavity [15]. Once the cavity is heated, the pressure increases and the diaphragm deflects. A thermopneumatic actuator based on printed circuit board (PCB) technology was developed at the University of Rostock,Germany [16]. The PCB used was 800 μm thick, connected to membrane consisting of polymeric foil of 8 μm thick. A special adhesive technique was utilized to connect the PCB with the membrane. A copper heater was used to facilitate the heat transfer to the actuator cavity. The measurements showed high volume displacement rates, up to 1000 μL/min, with large membrane deflection and moderate power consumption. However, neither the deflection nor the consumed power was mentioned in [16]. The main

advantages of a thermo-pneumatic actuator are the compatibility with MEMS fabrication, and the ability to produce large forces and deflection given very small volume [15] .

Phase change actuators are based on solid-solid [17] , solid-liquid [18] , and liquid-vapor [19] phase actuator. Generally, phase change actuators are characterized by the ability to produce high forces and displacements. The main drawback for those actuators is the slow response times [7].

The Shape Memory Alloy micro-actuators, (SMA) are considered superior in solid-solid actuation technology. The actuation mechanism of SMA , is the motion of those alloys due to phase transition between an austenite phase and a martensite phase [17]. This phase transition is governed by the temperature of the alloy. In [17], an SMA actuator [10 x 2 x 0.8] mm was built. A thermoelectric system was used to control the temperature of the SMA in the range -10 to 90 ^{o}C. The results showed that (4-6 %) strain is achievable. The main problem with SMA actuators is the cooling, especially when the environment temperature is not constant. Moreover, the dynamic response of SMA actuators is low and highly dependent on cooling abilities. In addition to that , SMA actuators are typically difficult to fabricate due to film stoichiometry or inherent stress problem [18].

The second kind of phase change actuators is solid-liquid phase change actuators. In this kind of actuator as the actuation layer is heated to its melting point, a volumetric expansion of that layer occurs. The volumetric expansion of that layer creates hydrostatic pressure which is translated to the output of the actuator. Paraffin is one of the most commonly used materials as the actuation layer in solid-liquid phase actuators due to its chemical stability and low viscosity [18]. In [18] paraffin microactuators were fabricated.

The actuators consisted of circularly patterned paraffin layers, 9 μm thick and 200-400 μm diameter, all covered with a 4 μm thick metallized sealing diaphragm. The actuators were constructed on both glass and silicon substrates. To achieve 2.7 μm peak deflection 100 mW power was input to a 200 μm radius actuator and 150 mW was input to 400 μm radius actuator. As it appears in this work, the main draw back of this kind of actuators is the large amount of power required to drive the actuator.

A similar actuation mechanism to solid- liquid phase change is the one due to phase change caused by liquid evaporation (liquid-vapor phase change). The volume expansion caused by liquid evaporation can generate considerable forces in small volume. In the literature many researchers have been investigating liquid-vapor phase change actuators. Paul *et al* [1] developed a thermally driven liquid- vapor phase change actuator in a partially filled- sealed cavity [900 x 900 x 300 μm in size]. A heater located on the floor of the cavity and elevated 8 μm above the cavity was 600 μm long and 800 μm wide. The heater was composed of diamond-shaped unit cells, 12 μm wide and 3 μm thick bulk silicon beams. Methanol was used to fill the cavity. An input power to the actuator of 10 mW caused a pressure rise in the cavity of 1.2 Atm. In a different reported measurement for an input power of 100 mW the pressure response time was around 100 ms.

Liwei Lin *et al.* [20] used 80 mW to generate a thermal bubble from *FC-43* liquid. The bubble was demonstrated to actuate a mechanical plate 70 x 60 x 2 μm with a maximum displacement of 140 μm and a maximum actuation force of 2 μN.

A comprehensive model for a thermo-pneumatic actuator was developed by Albert K. [19]. In this model, the change of phase from liquid to liquid-vapor, to vapor and back again was modeled. The thermodynamic model was coupled thermally and mechanically a

to silicon membrane microstructure. To define the initial thermodynamic state of the actuator the deflection of the midpoint of the membrane was assumed to be monotonic, the cavity was isobaric, isothermal under fill conditions, the vapor in the cavity obeyed the ideal gas law, and the external pressure on the membrane was uniform.

In addition to those assumptions, it was assumed that the deflection of the membrane was linear, and the working fluid in the cavity did not absorb any gas in the filling process. Based on those assumptions, the pressure on the membrane, the volume of the cavity, liquid density, vapor density and the total mass inside the cavity were estimated.

Under the assumption that the actuation occurs at constant temperature, the conservation of the mass inside the cavity, the conservation of volume in conjunction with the liquid pressure and densities were used to separate the volume into two parts, the volume occupied by the liquid and the one occupied by the vapor. The mechanical motion of the membrane and the pressure were then used to relate the membrane position to the valve flow. The model predictions showed good agreement with the measured data.

1.2 Micro Heat Engines

Several micro engines are proposed in the literature. One of those micro engines is the P^3 micro heat engine designed at Washington state university. The design of the P^3 micro heat engine is slightly different from all other micro engines. Other micro engines are based on miniaturization an internal combustion engine concept, while the P^3 micro heat engine is developed totally from the micro scale. The P^3 micro heat engine is an external combustion engine. The P^3 micro heat engine consists of two membranes separated by a thin cavity filled with a two-phase working fluid. The upper membrane is patterned with PZT to convert the mechanical work into electrical work. Heat is added to

the engine via a thermal switch. Once the heat is applied to the lower membrane the liquid inside the cavity evaporates. The volume expansion of the fluid in the cavity strains the upper membrane which results in the generation of electrical charge from the PZT. Heat is then removed with the thermal switch. The upper membrane cools and condensation occurs. The volume is decreased and the upper membrane deflects inward. The repetition of the cycle results in continuous process and charge generation.

A silicon-based micro rotary engine is being produced at U.C. Berkeley's microfabrication laboratory [21]. The ultimate goal of the work is to miniaturize a Wankel internal combustion engine to a micro engine that produces 10-100 mW while the size of the chamber is 1 cm^3 and the engine displacement is 0.08 m^3. As a pre-step the Wankel internal combustion engine was reduced to 1 cm^3 engine made of steel using electron discharge machining (EDM). The engine was operated using H_2-air mixture as the fuel at 10,000 rpm. The results showed that only 3.0 W output from the engine with efficiency less than 0.5%. The tests also showed that around 20% leakage happened while running the engine.

Later on, a micro heat engine consisting of three main parts, rotor, housing, and shaft, was fabricated. Each component was fabricated separately using different masks to simplify the fabrication process and to allow testing various engine parameters and designs. The engine housing consisted of 300 μm high housing with a spur gear ¼ to ½ the over all height of the housing wall. The rotor design consisted of gear sets ranging from 3-54 teeth. Deep Reactive Ion Etching (DRIE) was used to etch the spur gear and housing. The significant lateral etching in spur gear and the non uniform etch rate in the wafer reduced the number of usable parts and caused sealing problems. The work up to the moment on

this engine demonstrates that the sealing problem and friction losses are significant in this micro engine and a big challenge for miniaturization of Wankel internal combustion engine.

A MEMS-based gas turbine generator is being developed by researchers at MIT [22]. In this work, they try to scale the Brayton power cycle (gas turbine) down to the micro scale. The proposed engine is 1.0 cm diameter by 3.0 mm thick SiC and capable of producing 10-20 W of electric power while consuming 10.0 grams/hr of Hydrogen. The engine consists of conventional engine parts; compressor, combustion chamber and turbine. The efficiency of the combustion is estimated to be around 50% , and the mechanical to electrical conversion efficiency is 40%. Taking all the efficiencies in account, the estimated over all efficiency is around 5%. Many challenges for the design of this engine are currently under investigation. First, the complexity of geometry results in fabrication problems, for example, the tolerance of the bearing structures needs to be in the order of 1 μm. The journal bearings are required to be 300 μm deep and 10-20 μm wide with vertical taper less than 1 μm. The next challenge is the pressure and temperature of combustion. The operational temperature of the chamber is around 1000 ^{o}C. The pressure is going to be significant percentage of the bulk strength of silicon, and appreciable stresses are also generated in rotors due to the high spin speed [23]. More details about the history and development of micro heat engines is in [15, 21].

1.3 Objective of the work

The main objective of this work is to develop and validate a coupled dynamic, heat and mass transfer mathematical model to provide better understanding of the micro heat engine dynamic behavior. Understanding the dynamic behavior of the engine will allow minimizing the energy losses in the engine by optimizing the engine parameters. Those parameters include cavity thickness, bubble size, the upper and lower membrane size, and the heat rate delivered to the engine. Optimizing those parameters will increase the efficiency of the engine, and define the best conditions to operate the engine at, in terms of the duration of the heat pulse, and the cycle frequency.

Once the model is developed, it is validated against the experimental results. The validation of the model against the experimental results is important to ensure that the model captures the real physics of the engine. The model can then be used to predict the performance of the engine operated at different conditions and engine parameters.

To accomplish these goals, a device with a simplified geometry is modeled and characterized experimentally. This device, the cantilever engine, provides a valuable platform for model validation and also serves as a generic phase-change actuator.

Once the model is validated with experiments on the cantilever engine, the model is tested on the enclosed engine configuration. This configuration represents more closely the geometry of an actual micro heat engine.

CHAPTER 2

FABRICATION AND INSTRUMENTATION

Two different engines are presented in this work; the enclosed engine and the cantilever engine. In both engines, an evaporator is used to transfer the heat to the working fluid. However, the mechanical work is done on a silicon nitride membrane in the enclosed engine while it is done on a cantilever in the cantilever engine.

In the following sections, a detailed discussion of the engines fabrication is presented. The equipment used to test the engines is described, and the testing procedure for each engine is detailed.

2.1 Overall discussion of the cantilever engine

A cantilever engine basically consists of a cavity filled with a saturated, two-phase working fluid, bounded on the top by a microscope glass cover slip and on the bottom by a membrane patterned with a gold resistance heater to facilitate the heat transfer to the working fluid. The cover slip is bonded to a cantilever to provide additional mass and control the displacement of the cover slip. A schematic of the engine is shown in figure 2.1. The heater membrane is fabricated in the WSU –clean room facility as described in section 2.1.2.

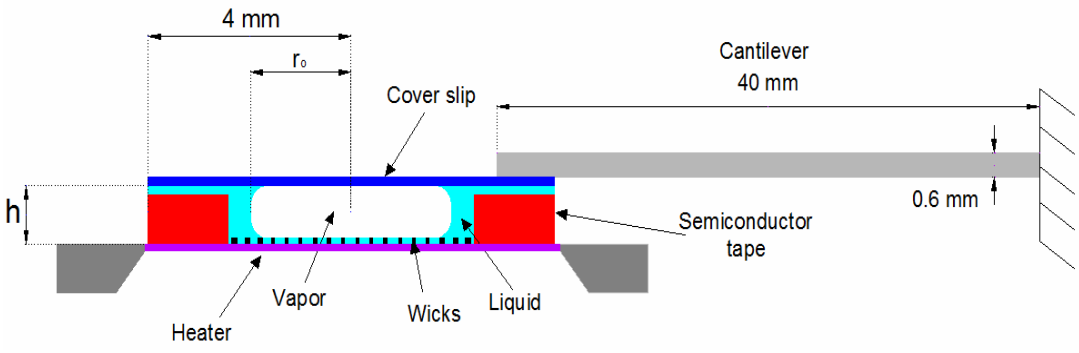

Fig 2.1: Cantilever Engine configuration.

The bottom membrane, which acts as an evaporator, is either 5 or 8 mm on a side. The gold layer is 300nm thick. A capillary wick structure is patterned over the heater to control the layer of liquid – phase working fluid. The wicks channels are 5 μm thick, 10 μm deep and 70 μm wide. The wicks and the heater cover the entire area of the bottom membrane. Figure 2.2 shows the heater and wick structure used in the cantilever engine.

The cavity is formed by adding very thin semiconductor tape layers together. Each layer is approximately 75 μm thick. The side length of each layer is almost the same as the side length of the bottom membrane.

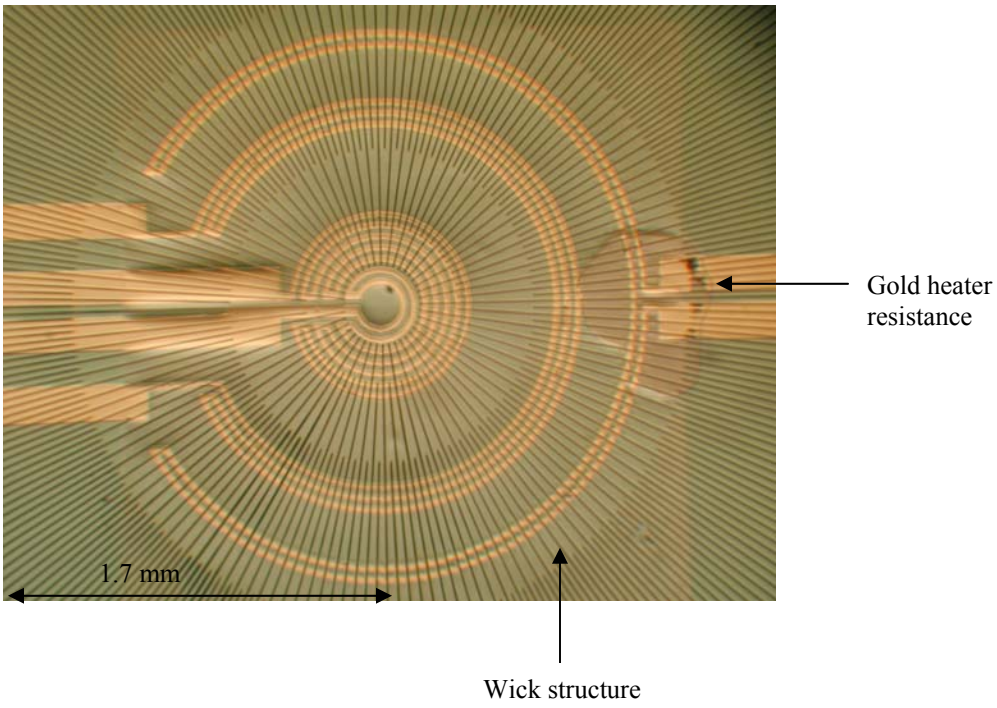

Fig 2.2: bottom membrane structure.

The cantilever consists of a thin copper electrode (0.6 mm) covered with upper and lower PZT layers to convert the mechanical work into electrical work. The resonant

frequency of the cantilever is altered by changing the free length of the cantilever. For the work done here, the free length was kept constant 40 mm.

2.1.1 Fabrication of the heater membrane

First a 3 inch wafer is oxidized in a high temperature wet oxidation process (T=1050 ^{o}C) for 80 min to grow 500 nm thick oxide layer. Next, boron is diffused at 1125 ^{o}C for 90 min. The importance of Boron is that, it slows down the etch rate of the anisotropic etching process by factor of 50 if the concentration of the boron is more than 5×10^{19} cm^{-3} . This is important to define the thickness of the membrane when etched. Then, subsequent minor steps are carried out to remove the borosilicate glass layer formed as result of Boron doping. Removal of this film includes a Buffer Oxide Etch (BOE) etching, sacrificial oxide growth, and a second BOE etch. A thin oxide layer which serves as an etch mask, is grown in a low temperature wet oxidation process (T=850 ^{o}C) for 80min. Then a 5 nm adhesion layer of TiW is sputtered on the silicon wafer followed by 300 nm and 500 nm Au layers sputtered on the front and back side of the wafer respectively. Next, both sides of the wafer are patterned using standard contact photolithography. The front side is patterned into a resistance heater. The back side is patterned into a silicon window membrane, it is important to keep the unpatterned gold on the backside protected when gold etchant is used to etch the front side. Later on, the remaining gold layer on the back side of the wafer serves as an etch mask. A SU-8 layer is spun over the resistance heater and patterned into wick structures. The wafer is etched in KOH at 80 ^{o}C for 6-8 hours. Figure 2.3 describes the general steps of heater fabrication

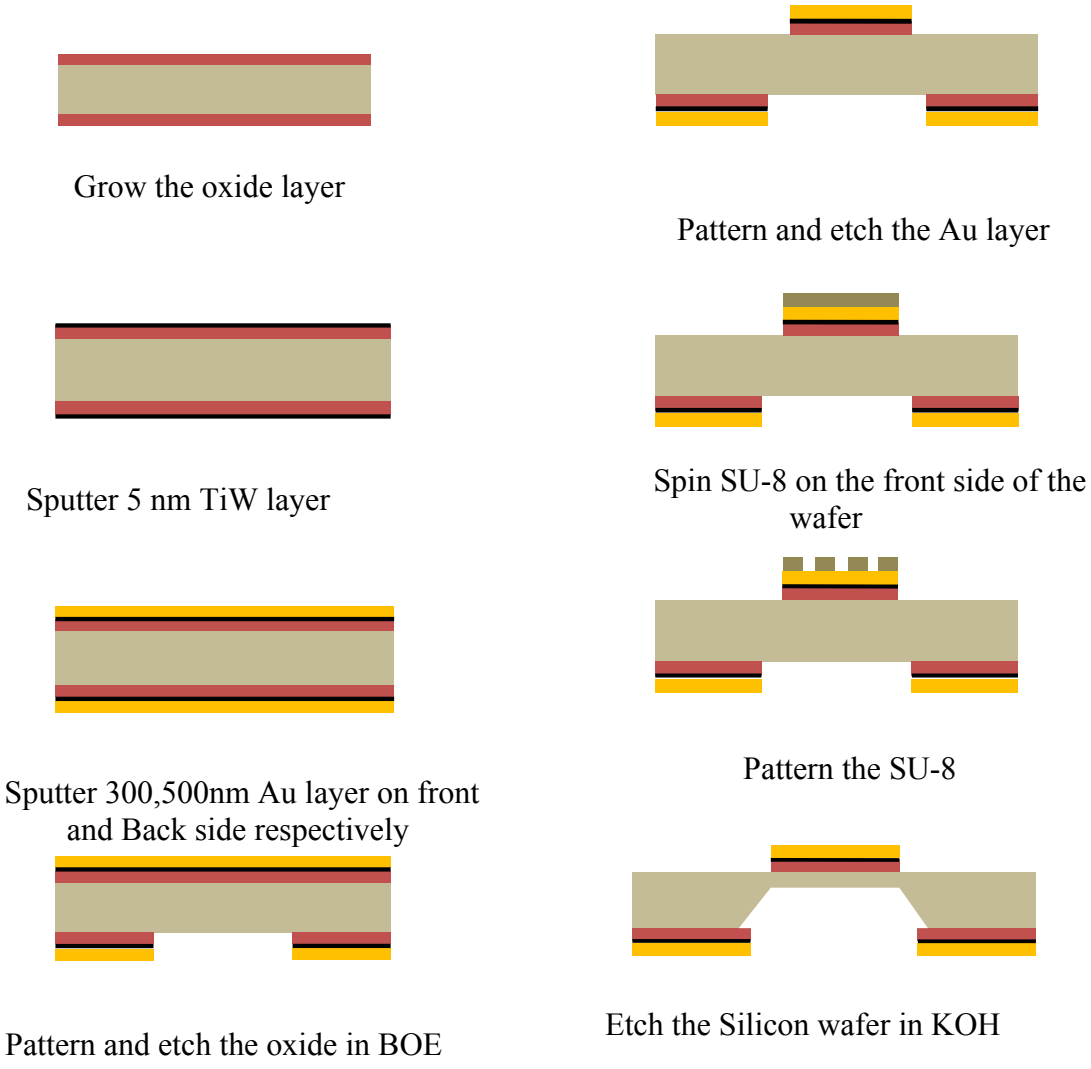

Fig 2.3: Heater membrane fabrication.

2.1.2 Engine Assembly

Once the heater with the desired size is fabricated in the clean room the cantilever engine is assembled. First, the heater die is fixed on a carrier plate. Semiconductor tape is cut out in two concentric square shapes and centered around the heater. Each semiconductor layer is 75 μm thick so the thickness of the engine is changed by changing the number of the layers attached to the top of the heater, when the layers are added

together it is important to ensure that there is no air gap between any two layers or between the first layer and the heater. This is important to keep the working fluid inside the engine during the whole experiment. Next, the cantilever is clamped to a holder and fixed onto a Z-stage. Since the quality factor (Q) is highly affected by the clamping conditions, Q should be characterized before running the experiment using an impedance analyzer.

Once both the cantilever and the heater are fixed on the stage. The working fluid FC-77 is flooded into the cavity and the cantilever is placed over the semiconductor layers by moving the Z position of the stage down. At this point a bubble is generated. The size of the bubble is controlled by the amount of time that the working fluid is allowed to evaporate before the engine is sealed by the liquid layer formed between the semiconductor tape and the cantilever.

2.1.3 Testing Procedure

Once the cantilever engine is sealed well, the operator can start the test. The resistance of the heater is measured. Figure 2.4 shows the experimental setup for testing the cantilever engine. The main parameters to be measured in the experiment are the size of the bubble, the vibration response of the cover slip, the open circuit voltage, and the output voltage across a load resistance when the PZT cantilever is hooked up to it. The size of the bubble is measured relative to the size of the heater membrane. The gold rings patterned on the heater membrane serve as good reference lines for bubble size measurements.

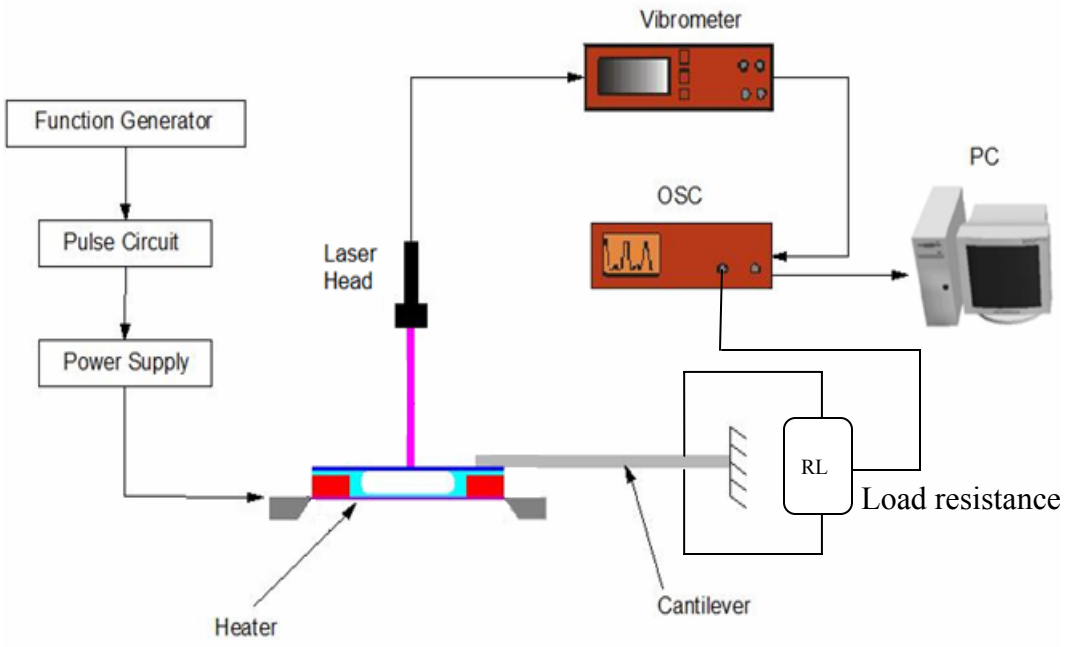

Fig . 2.4: Cantilever Engine experimental setup.

The vibration response of the cover slip is measured using a laser vibrometer. The settings of the laser vibrometer are chosen to yield in high sensitivity and low noise level. The vibration response is viewed on an oscilloscope screen. The oscilloscope outputs 2500 points for each screen capture. The settings of the oscilloscope are chosen to capture an integer number of cycles. For the highest resolution one cycle is the best. For example, if the engine is pulsed at 10 Hz, the number of the divisions on the oscilloscope is 10 divisions then 10msec/div is the setting on the oscilloscope to capture one cycle (2500 point on the oscilloscope screen). Capturing a non integer number of cycles on the oscilloscope screen results in wrong Fourier amplitude coefficients when analyzing the data.

2.2 EQUIPMENT

2.2.1 Laser Vibrometer

A laser Vibrometer is used to measure the displacement of the cover slip. The vibrometer used here is a Polytec OFV-5000. The operating principle of the laser vibrometer is Doppler shift of the laser light being reflected off the object. A beam of a helium neon laser is directed at the vibrating object and scattered back from it. The phase $\Delta\varnothing$, and frequency Δf information of the reflected beam are then recovered in signal processing unit using velocity and displacement decoders. The displacement signal is reconstructed from the phase information, while the velocity information is recovered from the frequency information. Figure 2.5 shows the working principle of the laser vibrometer.

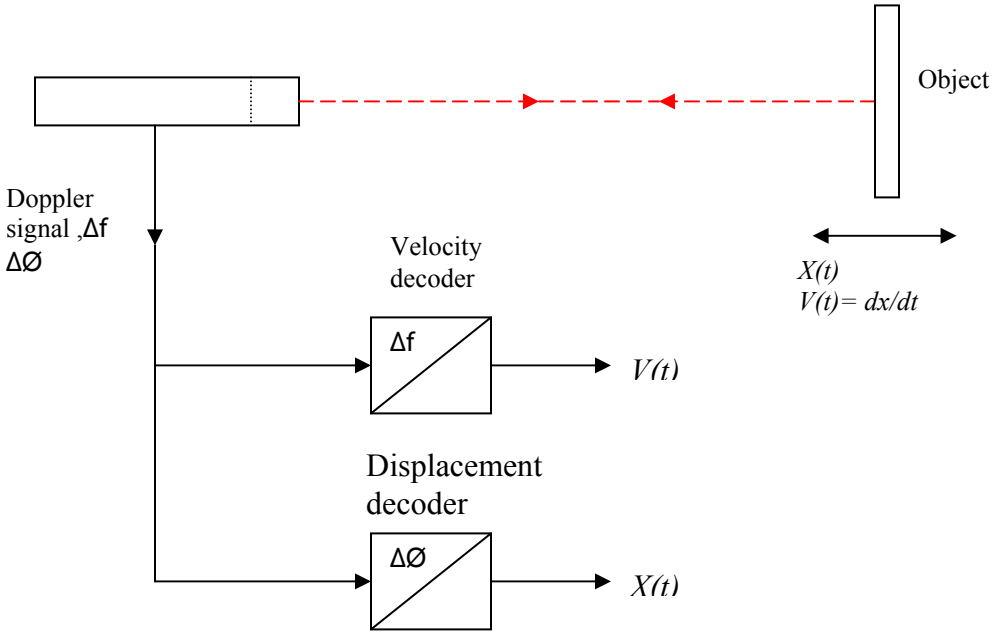

Fig 2.5: Working principle of Laser vibrometer [25].

2.2.2 TTL Circuit

A transistor-transistor logic (TTL) circuit [15] controls the voltage across the heater resistance based on trigger signal from arbitrary function generator (AFG). A schematic diagram of the TTL circuit is shown in figure 2.6, [15]. Detailed description of the TTL circuit is found in [15].

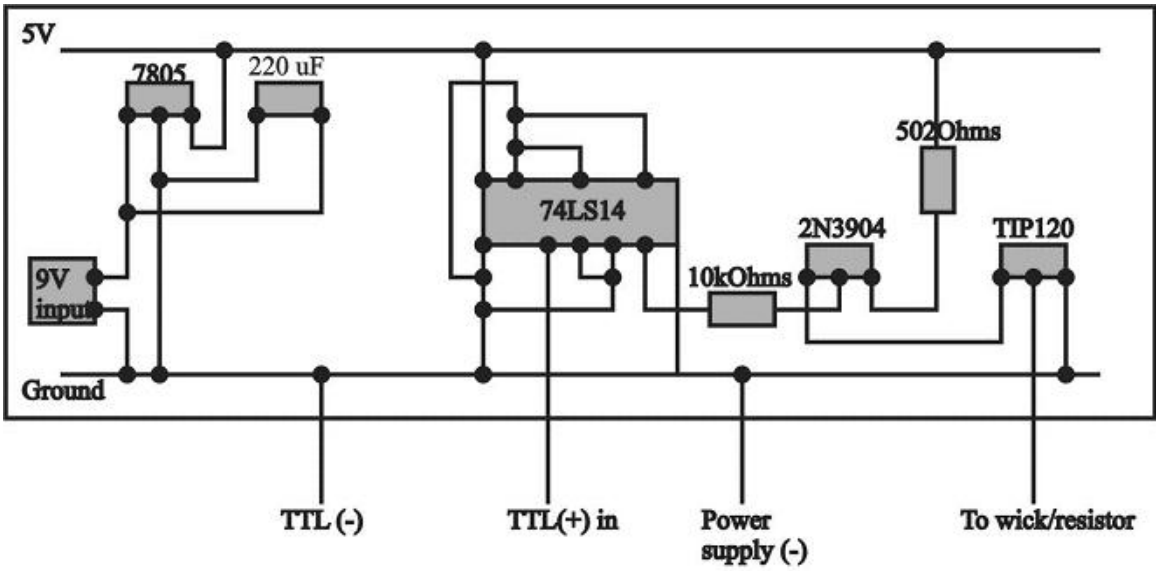

Fig. 2.6: TTL circuit [15].

2.2.3 Impedance Analyzer

The impedance and phase information are important to obtain the equivalent circuit parameters of the PZT cantilever, the quality factor, the electromechanical coupling coefficient and the natural frequency.

An Agilent A4294A impedance analyzer is used to measure the impedance and the phase of the cantilever engine. The frequency range of the Impedance analyzer is 40.0 Hz -

110.0 GHz, [26]. The input voltage level starts with few mvolts up to a maximum level of 1.0 volt.

2.2.4 Spectrum Analyzer

The Spectrum Analyzer used here is an Agilent 35670A. It is able to view the output signal form the laser vibrometer and analyze it directly. That is done by defining the signal as an independent variable and using it to write a mathematical function that describes the physical quantity the operator would like to see on the screen. An example for that is to define the electrical power across a resistor using the output voltage signal from the PZT cantilever.

Also, the spectrum analyzer has many built-in functions that help to understand the captured signal on the screen, one of the most useful functions is the Fast Fourier transformation (FFT) function used for frequency domain analysis.

2.2.5 Digital Oscilloscope

The main purpose of the oscilloscope is to view the output signal from the laser vibrometer and the output voltage from the cantilever. Once the desired signal is captured on the oscilloscope, it is saved on a volatile memory disk until the operator hits the start button again. The oscilloscope used here, TDS 420A, had 8 bit vertical resolution , maximum sampling rate of 200 MS/s , and 200 MHz bandwidth.

One of the important settings for these experiments is the COUPLING setting on the oscilloscope, that is, AC and DC coupling. When the engine is pulsed at a frequency higher than the cut-off frequency of the oscilloscope (8.0 Hz), use of the AC coupling won't affect the output signal that appears on the screen. However, if the engine is pulsed at a frequency lower than the cut-off frequency, it is important to set the oscilloscope to DC

coupling, otherwise all the frequency components lower than the cut-off frequency are filtered out and won't appear in the frequency domain analysis.

2.3 MEASUREMENT OF THE ENGINE PROPERTIES

2.3.1 Impedance test

The impedance analyzer is used to measure the impedance and the phase curves of the cantilever. A MATLAB program [24] is used to calculate the values of the equivalent circuit parameters from the impedance curve, including the natural frequency, the quality factor, and the electromechanical coupling coefficient.

To run an impedance test for a cantilever, first the impedance analyzer is calibrated by two tests, open and short compensation data measurement tests. Once it is calibrated, the cantilever is connected to the test fixture device contacts. The frequency bandwidth on the impedance analyzer screen should be chosen to capture the resonant frequency of the cantilever. For the experiments reported here the bandwidth was chosen to be 50.0 Hz-300.0 Hz, the voltage level used was 500 mvolts and 800 points were used to sample the impedance data. More detailed information on how to use the impedance analyzer is given in [24].

2.3.2 Stiffness measurement of the cantilever

The free vibration response of the cantilever in conjunction with the equivalent circuit parameters determined from an impedance test are used to calculate the stiffness of the cantilever. Since the impedance information is used in stiffness calculations, it is important to run the free vibration test under the same clamping conditions used to generate the impedance information.

For the free vibration test, the cantilever is pulsed for time duration much shorter than the natural period of the cantilever, the response of the cantilever is then captured by the laser vibrometer.

2.4 ENCLOSED ENGINE

An enclosed engine is defined by two membranes separated by a cavity filled with a two-phase working fluid. The upper membrane is usually a 2 μm thick silicon nitride membrane and the lower membrane is a bare silicon membrane. The lower membrane features are very similar to those used in the cantilever engine; that is, there is a wicking structure and a resistance heater.

The configuration of both the lower membrane and the semiconductor tape is the same as the one mentioned in section 2.1.1. The silicon nitride membrane used here is a bare membrane to allow the operator to see the bubble inside the engine. More generally, an energy converter, usually PZT , is patterned on the upper membrane to convert the mechanical work into electrical work.

The working fluid used to fill the cavity is PF-5060 by 3M®, which is characterized by a low boiling temperature (56^{o} C). The fact that PF-5060 starts evaporation at room temperature helps to generate the bubble as soon as PF-5060 is flooded into the engine.

2.4.1 Fabrication of Silicon Nitride membranes

A similar procedure to that described in section 2.1.2 is used to dope the boron to the silicon wafer. Consequently, a silicon nitride layer is grown on the front side of the silicon wafer. The silicon nitride is then patterned using the standard photolithography process and developed using KZ-400 solution. Figure 2.7 shows the oxide mask used to pattern 5 mm silicon nitride membranes. Then the nitride layer is patterned using Deep Reactive Ion

Etching (DRIE). Lastly, the wafer is etched in KOH solution to get 2 μm thick silicon nitride membranes.

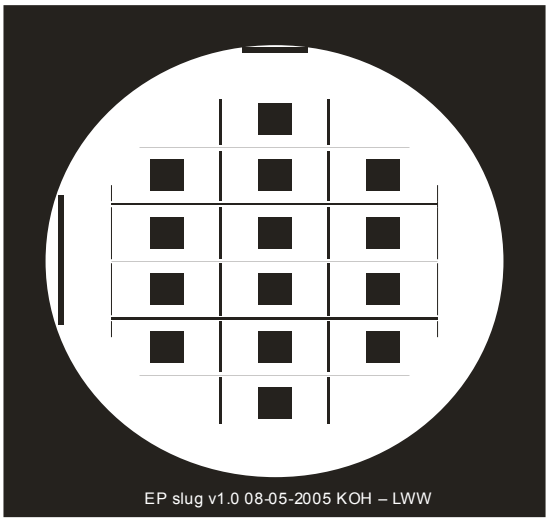

Fig. 2.7: 5mm silicon nitride membrane oxide mask.

2.4.2 Engine Assembly

Once the silicon nitride membrane and the heater membrane are fabricated, the engine can be assembled. The engine is defined by the thickness of the cavity, the size of the bubble, the size of both the heater membrane and the upper membrane and lastly, the wick structure patterned on the heater membrane.

First the heater membrane is fixed on a carrier plate. Then an o-ring is fixed on another plate, the upper membrane placed on the o-ring and taped to the plate. Next the semiconductor tape is cut out as two concentric squares and centered around the heater membrane. To build a thick engine, more layers of the semiconductor tape are cut out and placed on the top of each other. A heat sink compound may be used between the layers to

ensure good sealing. The PF-5060 is flooded to fill the cavity and the upper membrane is slid over the cavity. At this point the bubble is generated. The size of the bubble is determined by the amount of time PF-5060 is allowed to evaporate before the engine is sealed. Lastly, the upper carrier is screwed to the lower one and the plates are tightened good enough to seal the engine. If the carriers are tightened too much that might crack the engine. On the other hand, poor tightness might cause the engine to leak.

2.4.3 Measurement of the Upper membrane Stiffness

The stiffness of the upper membrane is measured experimentally by applying a uniform force over all the membrane area. A static bulge tester is used as the pressure source and the laser vibrometer is used to measure the peak deflection of the membrane.

First, the membrane die edges are carefully glued to a circular aluminum plate with a centered hole in it. Next, the plate is fixed on the static bulge tester and the laser beam is focused on the midpoint of the membrane. Then the pressure is applied. Both the pressure and the deflection are saved and plotted using a LabView program. The voltage signal from the laser vibrometer is converted directly to micrometers in this program; each volt from the laser vibrometer is interpreted as a deflection of 16 micrometer. For this reason, when running this experiment, it is important to use 16μm/volt on the laser vibrometer displacement settings.

2.4.4 Testing Procedure

Once a well sealed engine is assembled it is ready to be operated. The steps to operate the enclosed engine are generally the same as those used to operate the cantilever engine. The function generator is used to generate a square wave at the desired frequency and duty cycle. The TTL circuit controls the voltage across the heater resistance and the power

supply provides the engine with the required amount of energy. Figure 2.8 shows the experimental setup for the enclosed engine

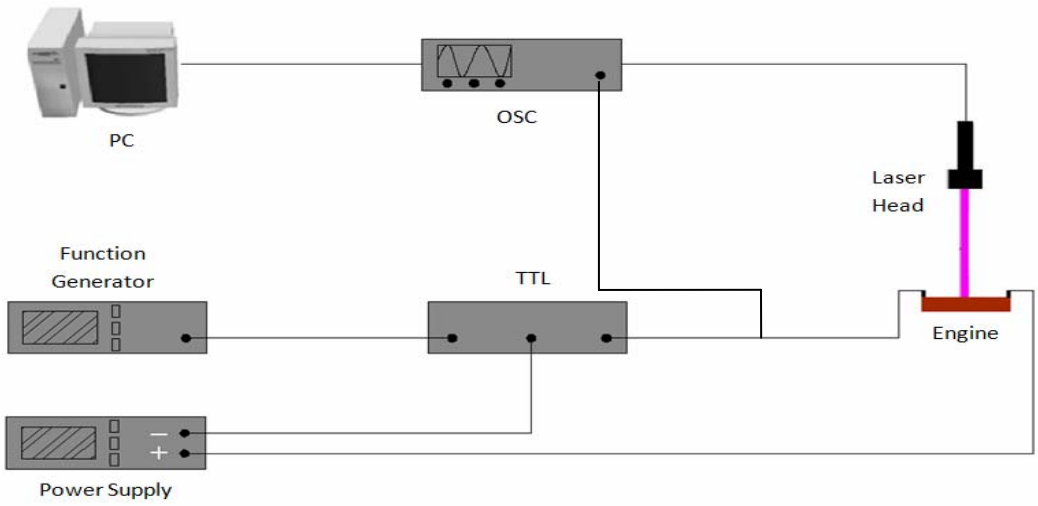

Fig. 2.8: Enclosed engine experimental setup.

The laser vibrometer is used to detect the deflection of the upper membrane. For the cases where the engine is excited at frequency lower than the cut–off frequency of the oscilloscope (8.0 Hz); a DC coupling should be used on the oscilloscope settings.

The time duration of the pulse is different from one experiment to another. For example, it is known that the response of the enclosed engine is slow. The roll-off frequency is around 2.0Hz. To capture the behavior of the engine around the roll off frequency the engine was excited at 0.2 Hz, 1% duty. In a different experiment the engine was excited at frequencies 10.0 Hz -100.0 Hz and the duty cycle range 1% -50% while the input energy was kept the same in all cases, to capture the amplitude distribution of the input heat spectrum over different bandwidths.

CHAPTER 3

MATHMATICAL MODELING OF A MICRO HEAT ENGINE

3.1 Introduction to the Model

Understanding the behavior of a designed device is crucial to predict the optimization of the device parameters for the best performance. In this work the energy conservation equations, Newton's second law and the conservation of mass equation are used to model a micro heat engine.

A mathematical model is developed to predict the deflection of the upper membrane, the temperature of the liquid, the pressure of the engine vapor and the output voltage from a mechanical to electrical energy converter.

The use of the energy and mass conservation equations in this model results in a nonlinear model. A linearized version is obtained by assuming the departures from the static values are very small.

A complex number analysis is used to solve the linearized model. A MATLAB program is used to implement this system of the linearized equations. In the following sections both the nonlinear and the linearized model are developed.

3.2 Geometry

A model schematic of the engine is shown in figure 3.1. The cavity of the engine is cylindrical in shape with radius r_o and nominal thickness h. In the cavity there is a central vapor bubble of radius r_i. Liquid occupies the remaining annulus. There is a film of small thickness at the bottom of the bubble. Liquid and vapor are at saturated equilibrium.

The top of the bubble is bounded by a movable rigid diaphragm of mass m constrained to move by a spring of stiffness s and a damper with coefficient b. From the bottom the bubble is bounded by a movable rigid heater constrained by the spring s_h. The motion of the upper and lower diaphragms is measured by the displacement x and x_h respectively. $T_o+\Delta T$, $P_o+\Delta P$, $\rho_o+\Delta\rho$ are the instantaneous temperature, pressure and density of the bubble. The instantaneous temperature of the liquid layer is given by $T_o+\Delta T_l$.

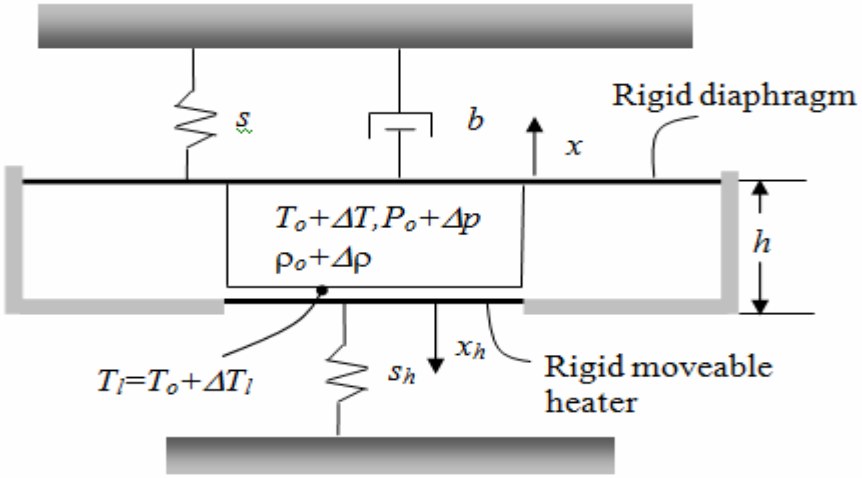

Fig. 3.1: Model engine schematic

3.3 Governing equations

The governing equations of the simplified version of the device shown in figure 3.1 are obtained by applying Newton's law for the motion of the upper and lower diaphragms, the conservation of the energy for the liquid layer and the bubble and conservation of mass in the bubble.

Applying the conservation laws results in nonlinear model of six equations with six unknowns. A linearized model is then obtained by making the assumption that the departures Δ from the static positions are negligible. For the dynamic analysis of the

system an electrical circuit analogy is used to represents the system of the linearized equations. A MATLAB program is then used to solve the linear system of equations using matrix and complex number analysis.

3.3.1 Mass transfer into the bubble

For a control volume bounding the bubble, shown in figure 3.2, conservation of mass requires

$$\frac{d}{dt}\left[(\rho_o + \Delta\rho)(V_o + \Delta V_g + \Delta V_h) \right] = \dot{m}, \tag{3.1}$$

where $\rho_o + \Delta\rho$, $V_o + \Delta V_g + \Delta V_h$ are the instantaneous vapor density and bubble volume respectively and $\dot{m}$ is the rate of mass transfer to the vapor bubble caused by evaporation and condensation of the liquid. The subscript "*o*" indicates an ambient and/or static component, while Δ indicates a departure from the ambient value. For the bubble volume the static volume V_o was $V_o=\pi r_o^2 h$, and ΔV_g and ΔV_h are contributions from the motion of the upper diaphragm and moveable heater respectively to the bubble volume.

For evaporation and condensation of the vapor. The Langmuir-Knudsen model is used [27]

$$\dot{m} = \beta S \sqrt{\frac{M}{2\pi R_u}} \left[\frac{p_l(T_o + \Delta T_l)}{\sqrt{T_o + \Delta T_l}} - \frac{P_o + \Delta p}{\sqrt{T_o + \Delta T}} \right]. \tag{3.2}$$

Here M is the molecular weight of the vapor, R_u=8.31 J/mol•K is the universal gas constant, $T_o + \Delta T_l$ is the temperature of the liquid, p_l is the saturation pressure of the liquid, β is the vaporization/condensation coefficient, and $S=\pi r_i^2$ is the area of the bottom surface of the vapor bubble. In this model, β is same for evaporation and condensation. In figure 3.2 m_i represents the mass of the evaporated liquid, while the mass of the condensed vapor is represented by m_o. The difference between these masses, given by 3.2, added to the

original mass of the vapor in the bubble is the actual mass of the bubble, represented by m_s in the graph.

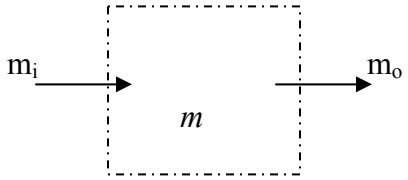

Fig . 3.2: Mass transfer into the bubble.

3.3.2 Conservation *of energy*

For a control volume bounding the bubble, shown in figure 3.3, conservation of the energy requires

$$\frac{d}{dt}\left[(\rho_o+\Delta\rho)c_v\left(V_o+\Delta V_g+\Delta V_h\right)(T_o+\Delta T)\right]=\dot{m}\left(u+\frac{P_o+\Delta p}{\rho_o+\Delta\rho}\right) -\left(P_o+\Delta p\right)\frac{d\left(V_o+\Delta V_g+\Delta V_h\right)}{dt}-U_B\Delta T \quad , \quad (3.3)$$

where u is the internal energy of mass transport associated with evaporation and condensation, and U_B is an overall heat transfer coefficient intended to account for heat transfer from the bubble to its surroundings. The internal energy flows into the bubble due to mass transfer is given by $\dot{m}u$. The flow work to account for transport of vapor into the bubble is given by $\dot{m}\,\frac{P_o+\Delta p}{\rho_o+\Delta\rho}$, and denoted by W1 in figure 3.3. The boundary work done by the upper membrane $\left(P_o+\Delta p\right)\frac{d\left(V_o+\Delta V_g+\Delta V_h\right)}{dt}$ is denoted by W2 in figure 3.3. The heat lost by bubble to the environment is given by $U_B\Delta T$. The vapor in the bubble is assumed to be governed by the ideal gas law

$$\rho_o + \Delta\rho = \frac{P_o + \Delta p}{R(T_o + \Delta T)} \ , \tag{3.4}$$

where $R=R_u/M$ is the mass-specific gas constant [28].

For the liquid layer between the vapor bubble and the bottom membrane, conservation of energy is given by

$$C_T \Delta \dot{T}_l = q(t) - U\Delta T_l - h_{fg}\dot{m} \quad , \tag{3.5}$$

where C_T is the modeled thermal inertia, U is an overall heat transfer coefficient intended to account for heat conduction loss from the heater to its immediate surroundings, h_{fg} is the latent heat of the liquid, and $q(t)$ is the heat added and removed from the engine.

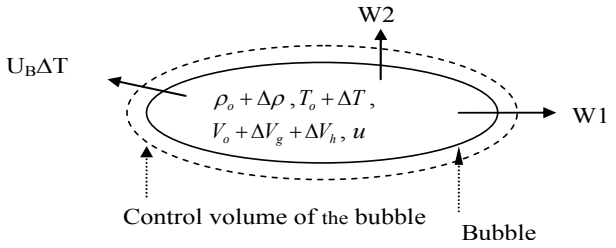

Fig. 3.3: Conservation of the energy in the bubble.

3.3.3 Newton's second law of the upper membrane

Applying Newton's law to the upper membrane, results in

$$(m+\bar{m})\Delta\ddot{x}+(b+\bar{b})\Delta\dot{x}+sx=\Delta p\pi r_o^2 \quad , \tag{3.6-a}$$

substituting for $x = \frac{\Delta V_g}{\pi r_o^2}$ in (3.6-a) gives

$$\frac{(m+\bar{m})}{(\pi r_o^2)^2}\Delta\ddot{V}_g+\frac{(b+\bar{b})}{(\pi r_o^2)^2}\Delta\dot{V}_g+\frac{s}{(\pi r_o^2)^2}\Delta V_g=\Delta p \quad , \tag{3.6-b}$$

where $\bar{m}$ and $\bar{b}$ are the effective mass and damping caused by liquid movements added to the upper diaphragm.

In a similar way, applying Newton's law to the bottom membrane, one obtains

$$\frac{s_h}{(\pi r_i^2)^2}\Delta V_h=\Delta p \quad , \tag{3.7}$$

where s_h is the stiffness of the bottom membrane, and r_i is the radius of the bottom membrane. For simplicity, the damping and material effects of the bottom membrane have been neglected in this equation. This is valid only if the frequency of the bottom membrane is much higher than the frequency of the upper membrane.

If a piezoelectric element is coupled to the flexible upper membrane, Newton's second law is modified to

$$\frac{(m+\bar{m})}{(\pi r_o^2)^2}\Delta\ddot{V}_g+\frac{(b+\bar{b})}{(\pi r_o^2)^2}\Delta\dot{V}_g+\frac{s}{(\pi r_o^2)^2}\Delta V_g+\frac{\psi}{\pi r_o^2}V=\Delta p, \tag{3.8-a}$$

where V is the voltage across the electrodes of the generator membrane, and ψ is the electrical-mechanical coupling (NV^{-1}). The deflection of the upper membrane is related to the voltage across the electrodes, given by

$$\frac{\pi r_o^2}{\psi}C_o\frac{d}{dt}\left[\frac{\psi}{\pi r_o^2}V\right]=-\frac{\frac{\psi}{\pi r_o^2}V}{\frac{\psi^2}{(\pi r_o^2)^2}R_L}+\Delta\dot{V}_g \quad , \tag{3.8-b}$$

where C_o is the capacitance of the piezoelectric element and R_L is the load resistance hooked up to the engine electrodes. In these formulas, it is assumed that there is a load resistance R_L between the electrodes of the piezoelectric element.

3.4 Development of Nonlinear Model

A nonlinear model of the engine is developed using set (3.1-3.8). The mass conservation law of the bubble is simplified by combining (3.1) and (3.2) , and eliminating ΔV_h using (3.7) to obtain

$$\Delta\dot{\rho}\left[V_o+\Delta V_g+\frac{(\pi r_i^2)^2}{s_h}\Delta p\right]+(\rho_o+\Delta\rho)\left[\Delta\dot{V}_g+\frac{(\pi r_i^2)^2}{s_h}\Delta\dot{p}\right]= \beta S\sqrt{\frac{M}{2\pi R_u}}\left[\frac{p_l(T_o+\Delta T_l)}{\sqrt{T_o+\Delta T_l}}-\frac{P_o+\Delta p}{\sqrt{T_o+\Delta T}}\right] \tag{3.9}$$

For the energy conservation of the bubble taking the derivative of (3.3) yields

$$c_v(T_o+\Delta T)\frac{d}{dt}\left[(\rho_o+\Delta\rho)\left(V_o+\Delta V_g+\Delta V_h\right)\right]+(\rho_o+\Delta\rho)(V_o+\Delta V_g+\Delta V_h)\frac{d}{dt}\left[c_v(T_o+\Delta T)\right] = \dot{m}\left(\frac{P_o+\Delta p}{\rho_o+\Delta\rho}\right)+\dot{m}u \quad -(P_o+\Delta p)\frac{d\left(V_o+\Delta V_g+\Delta V_h\right)}{dt}-U_B\Delta T \tag{3.10}$$

Then (3.1) is used to eliminate $\dot{m}$ from (3.10) to result in

$$\left[(\rho_o+\Delta\rho)\left(V_o+\Delta V_g+\Delta V_h\right)c_v\frac{d}{dt}(T_o+\Delta T)\right]=\dot{m}\left(\frac{P_o+\Delta p}{\rho_o+\Delta\rho}\right) -(P_o+\Delta p)\frac{d\left(V_o+\Delta V_g+\Delta V_h\right)}{dt}-U_B\Delta T \tag{3.11}$$

Eliminating $\dot{m}$ and ΔV_h from (3.11) using (3.1) and (3.7) respectively results in

$$\left[(\rho_o+\Delta\rho)\left(V_o+\Delta V_g+\frac{(\pi r_i^2)^2}{s_h}\,\Delta p\right)c_v\left(\dot{\Delta T}\right)\right]-\left(V_o+\Delta V_g+\frac{(\pi r_i^2)^2}{s_h}\,\Delta p\right)\left(\frac{P_o+\Delta p}{\rho_o+\Delta\rho}\right)\dot{\Delta\rho}=-U_B\Delta T \quad . \quad (3.12)$$

Eliminating $\dot{m}$ from (3.5) using (3.2) results in the following form of the energy equation of the liquid layer between the bubble and the heater

$$C_T\Delta\dot{T}_l=q(t)-U\Delta T_l-h_{fg}\,\beta S\sqrt{\frac{M}{2\pi R_u}}\left[\frac{p_l(T_o+\Delta T_l)}{\sqrt{T_o+\Delta T_l}}-\frac{P_o+\Delta p}{\sqrt{T_o+\Delta T}}\right]. \quad (3.13)$$

For the ideal gas, taking the derivative of (3.4) results in

$$\dot{\Delta\rho}=-\left[\frac{P_o+\Delta p}{R(T_o+\Delta T)^2}\right]\dot{\Delta T}+\frac{1}{R(T_o+\Delta T)}\dot{\Delta p} \quad . \quad (3.14)$$

Newton's law for the upper membrane is given by

$$\frac{(m+\bar{m})}{(\pi r_o^2)^2}\Delta\ddot{V}_g+\frac{(b+\bar{b})}{(\pi r_o^2)^2}\Delta\dot{V}_g+\frac{s}{(\pi r_o^2)^2}\Delta V_g+\frac{\psi}{\pi r_o^2}V=\Delta p\,. \quad (3.8\text{-a})$$

The piezoelectric material electrical-mechanical coupling is given by

$$\frac{\pi r_o^2}{\psi}C_o\frac{d}{dt}\left[\frac{\psi}{\pi r_o^2}V\right]=-\frac{\frac{\psi}{\pi r_o^2}V}{\frac{\psi^2}{(\pi r^2{}_o)^2}R_L}+\dot{\Delta V}_g \quad . \quad (3.8\text{-b})$$

The set (3.8,3.9, & 3.12,3-14) represent the complete nonlinear model of six equations and six unknowns Δp, ΔT, ΔV_g, ΔT_l, V and $\Delta\rho$.

3.5 Linearization of the model

A linear version of the model is obtained if the departures Δ of each quantity from their static values are very small. A linearized form of the Langmuir evaporation condensation model in (3.2) is obtained using Taylor series expansion, and applying Antoine correlation give by

$$\log(p_l) = \hat{A} - \frac{\hat{B}}{T_l + \hat{C}},$$

where $\hat{A}$, $\hat{B}$, and $\hat{C}$ are constants for the particular working medium. The linearized form of Langmuir evaporation condensation model in (3.2) is given by

$$\dot{m} = \beta S \sqrt{\frac{M}{2\pi R_u}} \left[\frac{p_l(T_o + \Delta T_l)}{\sqrt{T_o + \Delta T_l}} - \frac{P_o + \Delta p}{\sqrt{T_o + \Delta T}} \right] \approx$$

$$B \Delta T_l - \beta S \sqrt{\frac{M}{2\pi R_u}} \frac{1}{\sqrt{T_o}} \Delta p + \beta S \sqrt{\frac{M}{2\pi R_u}} \frac{\bar{\rho} \bar{R}}{2\sqrt{T_o}} \Delta T \quad , \tag{3.15}$$

where B is given by

$$B = \beta S \sqrt{\frac{M}{2\pi R_u}} \frac{10^{\bar{A} - \frac{\bar{B}}{T_o + \bar{C}}}}{\sqrt{T_o}} \left[\frac{\bar{B} \ln 10}{(T_o + \bar{C})} - \frac{1}{2T_o} \right] . \tag{3.16}$$

A linearized version of (3.1) is:

$$\dot{m} = \frac{d}{dt}\left[(\rho_o + \Delta\rho)(V_o + \Delta V_g + \Delta V_h) \right] \approx (\rho_o) \left(\Delta \dot{V}_g + \frac{(\pi r_i^2)^2}{s_h} \Delta \dot{p} \right) + \Delta \dot{\rho} V_o \ . \tag{3.17}$$

For the ideal gas (3.14) a linear approximation is given by

$$\Delta\rho = \frac{P_o}{R(T_o^2)} \Delta T + \frac{1}{RT_o} \Delta p \quad . \tag{3.18}$$

Substitution of (3.15) in (3.17) and using the linearized version of the ideal gas (3.18), results in a linearized version of the mass conservation of the bubble given by

$$\Delta \dot{V}_g + \left(\frac{V_o}{\rho_o R T_o} + \frac{(\pi r_i^2)^2}{s_h} \right) \Delta \dot{p} - \frac{V_o}{T_o} \Delta \dot{T} =$$

$$B \Delta T_l - \frac{\beta S}{\rho_o} \sqrt{\frac{M}{2\pi R_u}} \frac{1}{\sqrt{T_o}} \Delta p + \frac{\beta S}{\rho_o} \sqrt{\frac{M}{2\pi R_u}} \frac{\bar{\rho R}}{2\sqrt{T_o}} \Delta T \quad . \qquad (3.19)$$

A linearized version of the energy conservation for the liquid layer is give by

$$C_T \Delta \dot{T}_l = q(t) - U \Delta T_l - h_{fg} B \beta S \sqrt{\frac{M}{2\pi R_u}} \Delta T_l + h_{fg} \beta S \sqrt{\frac{M}{2\pi R_u}} \frac{\gamma + 1}{2\gamma \sqrt{T_o}} \Delta p \quad . (3.20)$$

A linearized version of the energy conservation for the bubble is given by

$$\frac{V_o}{T_o} \Delta \dot{T} - \frac{V_o}{\rho_o c_p T_o} \Delta \dot{p} = -\frac{U_B}{\rho_o c_p T_o} \Delta T \quad . \qquad (3.21)$$

The set (3.8 a & b, & 3.19-3.21) represent a linear set of five equations for five unknowns (ΔV_g , Δp, ΔT , V and ΔT_l). The set of the nonlinear and linear model are now given by

a- Nonlinear set

$$\frac{(m + \bar{m})}{(\pi r_o^2)^2} \Delta \ddot{V}_g + \frac{(b + \bar{b})}{(\pi r_o^2)^2} \Delta \dot{V}_g + \frac{s}{(\pi r_o^2)^2} \Delta V_g + \frac{\psi}{\pi r_o^2} V = \Delta p \quad , \qquad (3.8\text{-a})$$

$$\frac{\pi r_o^2}{\psi} C_o \frac{d}{dt} \left[\frac{\psi}{\pi r_o^2} V \right] = -\frac{\frac{\psi}{\pi r_o^2} V}{\frac{\psi^2}{(\pi r^2{}_o)^2} R_L} + \Delta \dot{V}_g \quad , \qquad (3.8\text{-b})$$

$$\Delta \dot{\rho} \left[V_o + \Delta V_g + \frac{(\pi r_i^2)^2}{s_h} \Delta p \right] + (\rho_o + \Delta \rho) \left[\Delta \dot{V}_g + \frac{(\pi r_i^2)^2}{s_h} \Delta \dot{p} \right] =$$

$$\beta S \sqrt{\frac{M}{2\pi R_u}} \left[\frac{p_l (T_o + \Delta T_l)}{\sqrt{T_o + \Delta T_l}} - \frac{P_o + \Delta p}{\sqrt{T_o + \Delta T}} \right] \quad , \qquad (3.9)$$

$$\left[(\rho_o+\Delta\rho)\left(V_o+\Delta V_g+\frac{(\pi r_i^2)^2}{s_h}\Delta p\right)c_v\left(\Delta\dot{T}\right)\right]-\left(V_o+\Delta V_g+\frac{(\pi r_i^2)^2}{s_h}\Delta p\right)\left(\frac{P_o+\Delta p}{\rho_o+\Delta\rho}\right)\Delta\dot{\rho}=-U_B\Delta T \quad , \quad (3.12)$$

$$C_T\Delta\dot{T}_l=q(t)-U\Delta T_l-h_{fg}\,\beta S\sqrt{\frac{M}{2\pi R_u}}\left[\frac{p_l(T_o+\Delta T_l)}{\sqrt{T_o+\Delta T_l}}-\frac{P_o+\Delta p}{\sqrt{T_o+\Delta T}}\right] \quad , \quad (3.13)$$

$$\Delta\dot{\rho}=-\left[\frac{P_o+\Delta p}{R(T_o+\Delta T)^2}\right]\Delta\dot{T}+\frac{1}{R(T_o+\Delta T)}\Delta\dot{p} \quad , \quad (3.14)$$

b- Linear set

$$\frac{(m+\bar{m})}{(\pi r_o^2)^2}\Delta\ddot{V}_g+\frac{(b+\bar{b})}{(\pi r_o^2)^2}\Delta\dot{V}_g+\frac{s}{(\pi r_o^2)^2}\Delta V_g+\frac{\psi}{\pi r_o^2}V=\Delta p \quad , \quad (3.8\text{-a})$$

$$\frac{\pi r_o^2}{\psi}C_o\frac{d}{dt}\left[\frac{\psi}{\pi r_o^2}V\right]=-\frac{\frac{\psi}{\pi r_o^2}V}{\frac{\psi^2}{(\pi r^2{}_o)^2}R_L}+\Delta\dot{V}_g \quad , \quad (3.8\text{-b})$$

$$\Delta\dot{V}_g+\left(\frac{V_o}{\rho_o RT_o}+\frac{(\pi r_i^2)^2}{s_h}\right)\Delta\dot{p}-\frac{V_o}{T_o}\Delta\dot{T}=$$

$$B\,\Delta T_l-\frac{\beta S}{\rho_o}\sqrt{\frac{M}{2\pi R_u}}\frac{1}{\sqrt{T_o}}\Delta p+\frac{\beta S}{\rho_o}\sqrt{\frac{M}{2\pi R_u}}\frac{\bar{\rho}R}{2\sqrt{T_o}}\Delta T \quad , \quad (3.19)$$

$$C_T\Delta\dot{T}_l=q(t)-U\Delta T_l-h_{fg}B\beta S\sqrt{\frac{M}{2\pi R_u}}\Delta T_l+h_{fg}\beta S\sqrt{\frac{M}{2\pi R_u}}\frac{\gamma+1}{2\gamma\sqrt{T_o}}\Delta p \quad , \quad (3.20)$$

$$\frac{V_o}{T_o}\Delta\dot{T}-\frac{V_o}{\rho_o c_p T_o}\Delta\dot{p}=-\frac{U_B}{\rho_o c_p T_o}\Delta T \quad , \quad (3.21)$$

3.6 Reduced Linearized Model, no heat transfer from the bubble (U_B=0)

The linearized model can be further reduced if the heat transfer from the bubble is neglected. For the case where $U_B=0$, (3.21) is reduced to

$$\rho_o c_v\,\Delta\dot{T}=\Delta\dot{p}\,. \quad (3.22)$$

Equation (3.22) is then used to eliminate the temperature ΔT from (3.19), which results in the following set of linear equations

$$\bar{C}_o \frac{d}{dt}\left[\frac{\psi}{\pi r_o^2} V\right] = -\frac{\frac{\psi}{\pi r_o^2} V}{\bar{R}_l} + \Delta \dot{V}_g \qquad (3.8\text{-b})$$

$$\frac{(m+\bar{m})}{(\pi r_o^2)^2}\Delta \ddot{V}_g + \frac{(b+\bar{b})}{(\pi r_o^2)^2}\Delta \dot{V}_g + \frac{s}{(\pi r_o^2)^2}\Delta V_g + \frac{\psi}{\pi r_o^2} V = \Delta p \qquad (3.8\text{-b})$$

$$C_T \Delta \dot{T}_l = q(t) - U\Delta T_l - h_{fg} B\beta S\sqrt{\frac{M}{2\pi R_u}}\Delta T_l + h_{fg}\beta S\sqrt{\frac{M}{2\pi R_u}}\frac{\gamma+1}{2\gamma\sqrt{T_o}}\Delta p \qquad (3.20)$$

$$\bar{C}\,\Delta \dot{p} = -\Delta \dot{V}_g - \frac{1}{\bar{R}}\Delta p + \frac{B}{\rho_o}\Delta T_l \quad , \qquad (3.24)$$

where:

$$\bar{C} = \frac{(\pi r_i^2)^2}{s_h} + \frac{V_o}{\gamma \rho_o R T_o}$$

$$\frac{1}{\bar{R}} = \frac{\beta S}{\rho_o}\sqrt{\frac{M}{2\pi R_u}}\frac{\gamma+1}{2\gamma\sqrt{T_o}} \qquad \bar{C}_o = \frac{(\pi r_o^2)^2}{\psi^2} C_o \qquad \bar{R}_l = \frac{(\pi r_o^2)^2}{\psi^2} R_l$$

$$\gamma = \frac{c_p}{c_v}, \qquad c_p - c_v = R$$

The set (3.6, 3.8, 3.20, 3.24) represent a linear set of four equations for four unknowns (ΔV_g, Δp, V and ΔT_l).

3.7 Electrical circuit analogy

Mechanical and electrical systems are considered to be analogous if both are described by the same differential equation. In most cases the goal is to represent the mechanical system by an equivalent electrical circuit. The benefit of such representation is that it is

easier to analyze and compute the dynamic behavior of a mechanical system using its equivalent circuit.

In general, two different analogies between electrical and mechanical systems are used, the impedance analogy and the mobility analogy

In the impedance analogy a force is the analog to a voltage (potential) and a velocity is an analog to the current (flux). In the mobility analogy a force is an analog to a current (flux) and a velocity is an analog to a voltage (Potential). Table 3.1 summarizes the analogous quantities for both methods. For the work presented here the impedance analogy was used to represent the mechanical system described by the linear set of equations mentioned in section 3.5. In the following sections the electrical circuit analogy is developed for the model.

Electrical Quantity	Mobility Analogy/Mech	Impedance Analogy/Mech
Voltage	Velocity	Force
Current	Force	Velocity
Resistance	Lubricity (inverse damping)	Damping
Capacitance	Mass	Compliance
Inductance	Compliance	Mass

Table 3.1: Electrical-Mechanical systems analog.

3.7.1 Electrical circuit analogy of the model with PZT

The equivalent circuit of the linearized model described in 3.5 is shown in figure 3.3. In this model, the thermal storage and the energy losses from the bubble are neglected C_T , $U_B = 0$ respectively. The unit of the current is volume flow rate (m^3 /sec) and the unit of the equivalent volts is pressure ($N.m^{-2}$), the product of the two quantities has units of power.

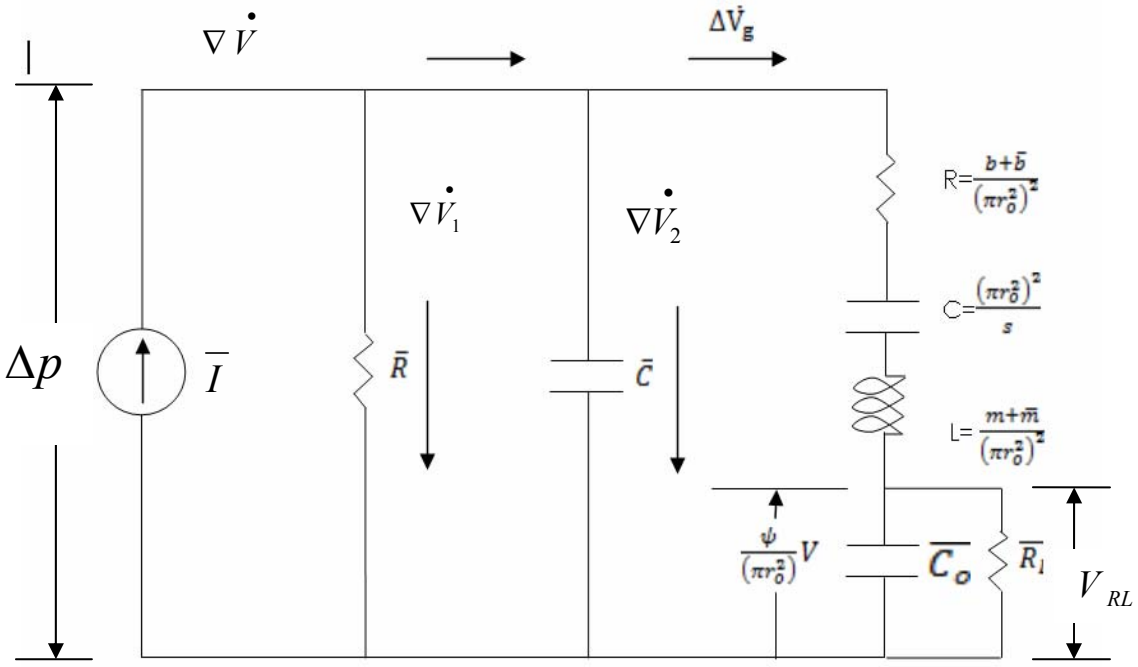

Fig . 3.3:Equivalent circuit of the linearized model with PZT energy converter.

In figure 3.3 , R,L,and C are the mechanical resistance, inductance ,and capacitiance respectivly. The mechanical resisitance R is dependent on the total damping characterstic $(b+\bar{b})$ of the engine. The mechanical inductace L is proportional to the effective mass of

the engine, given by ($m+\bar{m}$), while the stiffness s sets the mechanical capactiance C. The capacitance $\bar{C}_o$ is proportional to the shunt capacitance of the PZT element and given by $\bar{C}_o = \frac{\left(\pi r_o^2\right)^2}{\psi^2} C_o$. The linear set (3.8 & 3.19-3.21) are used to obtain the equivalent circuit of the linear model. The right circuit branch, given by the mechanial compnents RLC , and the shunt resistance $\bar{C}_o$ is obtained dirctly from 3.8-a. The load resistance $\bar{R}_L$ represents an external resistance connected across the cantilever to measure the output voltage. Equation (3.19) is used to obtain the branch of $\bar{R}$ and $\bar{C}$, where $\frac{1}{\bar{R}} = \frac{U/h_{fg}B}{U/h_{fg}B+1} \frac{\beta S}{\rho_o} \sqrt{\frac{M}{2\pi R_u}} \frac{\gamma+1}{2\gamma\sqrt{T_o}}$, and $\bar{C} = \frac{\left(\pi r_i^2\right)^2}{s_h} + \frac{V_o}{\gamma \rho_o R T_o}$. The flow rate $\nabla \dot{V}$ (m^3 /sec) is split into $\nabla \dot{V}_1$ which goes into $\bar{R}$, $\nabla \dot{V}_2$ which goes into $\bar{C}$, and $\nabla \dot{V}_g$ which is the volume rate change in the generator membrane. The current source is given by $\bar{I} = \frac{B}{\rho_o} \Delta T_l$.

The power dissipated across the load resistance $\bar{R}_L$, is given by

$$\prod_{Rl} = \frac{\left|V_{RL}\right|^2}{2\bar{R}_L}, \tag{3.25}$$

where $\prod_{RL}$ is the power dissipated in $\bar{R}_L$, V_{RL} is the voltage across the load resistance $\bar{R}_L$ given by

$$\frac{V_{RL}}{V} = \frac{Z_t}{(Z_t + Zm)} \quad ,$$

and the impedance Z_t and Z_m are given by

$$Z_t = \frac{1}{(j\omega \bar{C}_o + \frac{1}{\bar{R}_L})} \quad , \quad Z_m = j\omega L + R + \frac{1}{j\omega C} \ .$$

3.7.2 Electrical circuit analogy of the model without PZT

Fig 3.4 shows the equivalent circuit of the model without PZT. The power dissipated in R is used to simulate an energy conversion device.

The power across R is given by:

$$\prod_R = \frac{1}{2} RE \left[V_R \cdot \left(\frac{Y_m}{Y_T} \right)^* I^* \right] , \tag{3.26}$$

where V_R is the voltage across R given by

$$V_R = \frac{R}{j\omega L + R + \frac{1}{j\omega C}} V \quad ,$$

And the admittance Y_m, and Y_T are given by

$$Y_m = \frac{1}{j\omega L + R + \frac{1}{j\omega C}} \quad , \quad Y_T = Y_m + \frac{1}{\bar{R}} + j\omega \bar{C} \, .$$

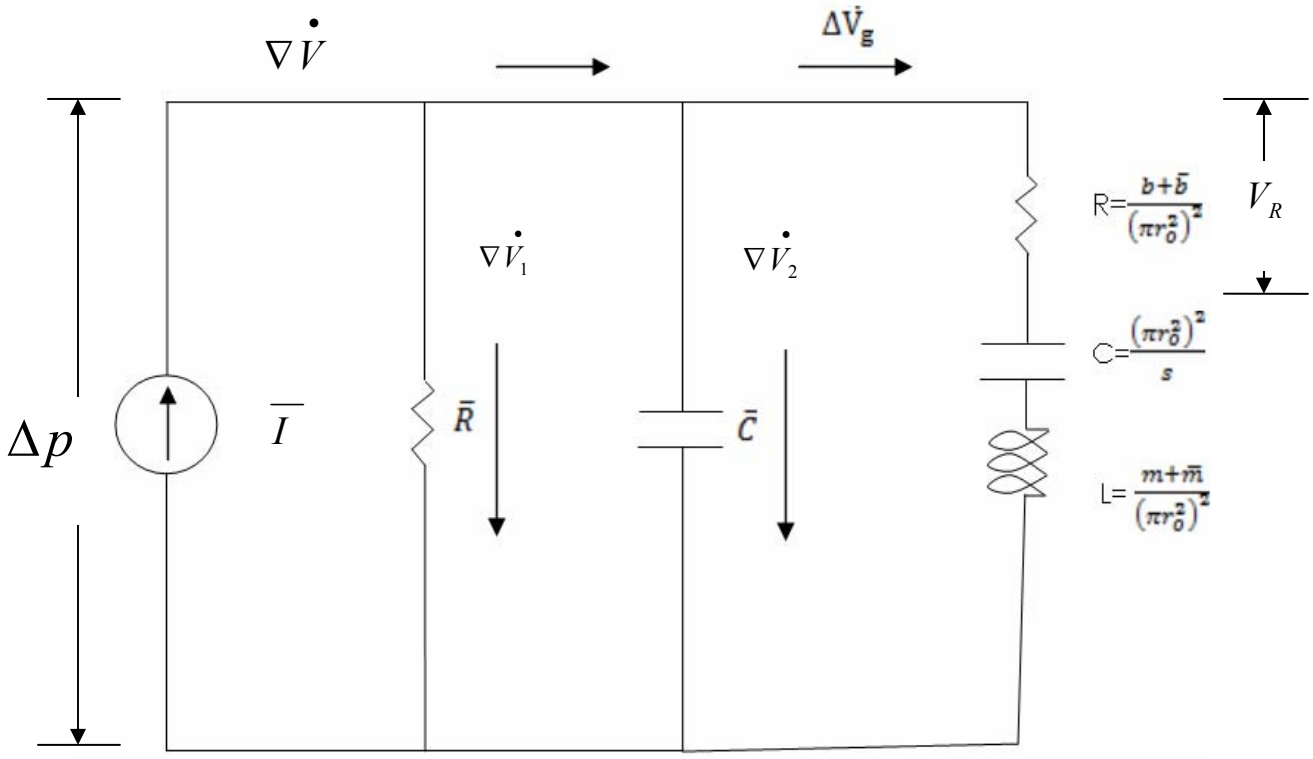

Fig 3.4: Equivalent circuit of the linearized model without PZT.

3.8 Solution of the linear system of equations

For the linear system of equations described in section 3.5, a state space representation of the six state equations are given by:

$$[A]\left\{\dot{X}\right\} = [B]\{X\} + \{C\}q(t) \quad , \tag{3.27}$$

where the state variables are given by

$$\{X\} = \begin{Bmatrix} \Delta V_g \\ \Delta \dot{V}_g \\ \Delta p \\ \Delta T \\ \frac{\psi}{\pi r_o^{\,2}} V \\ \Delta T_l \end{Bmatrix} .$$

The coefficient matrices $[A]$ and $[B]$ are the coefficient matrices of the unknowns column vectors $\{X\}$ and $\left\{\dot{X}\right\}$ respectively, and the column vector $\{C\}$ represents the coefficients of the input heat to the system $q(t)$. The solution of the system is assumed to be in the form of $X_i = \hat{X}_i e^{j\omega t}$, (3.28)

and then the derivative of the column vector $\{X\}$ is given by

$$\dot{X} = j\omega \left\{ \hat{X} \right\} e^{j\omega t} \quad . \tag{3.29}$$

For more details on the solution of the system of linear equations described in 3.5 see Appendix A.

CHAPTER 4

DATA ANALYSIS

Once the experimental data are collected, a fast Fourier transform (FFT) algorithm is used to analyze them. The least squares method (LSM) is then used to predict the unknown modele parameters and fit the model with the experimental data. The effect of the pulse duration, and the input heat rate distribution over the frequency components on the engine performance is predicted by Pareseval's theorem. In this chapter, a brief description of the FFT algorithm, LSM, and Pareseval's theorem are presented.

4.1 Fast Fourier Transformation (FFT)

Fourier transform, named after the French mathematician Joseph Fourier, is a mathematical tool to write any periodic function by decomposing such function into a weighted sum of a sinusoidal component functions referred to as modes [30]. For a continuous signal a Fourier transform is given by

$$\hat{X}(f) = \int_{-\infty}^{+\infty} x(t) \exp(-j2\pi ft)\ dt \tag{4.1}$$

where *x(t)* is a continuous-time signal and f is the transform variable with the units of Hz.

In most applications, the signal to be processed is sampled with a finite number of points (N), called discrete signal, the corresponding Discrete Fourier Transform (DFT) is given by

$$\hat{X}_k = \sum_{n=0}^{N-1} x_n . \exp(-\frac{j2\pi kn}{N}) \quad , \text{n} , k=0,1,2,\ldots\ldots,\text{N-1} , \tag{4.2}$$

the coefficients $\hat{X}_k$ are in general complex valued, and known as the DTF coefficients, x_n are the sampled data points, and Δt is the sampling interval. In this case, the fundamental data period $T_p = N.\Delta t$ is the reciprocal of the fundamental frequency f_p with units of Hz.

If the number of the data points (N) is an even power of 2^P (P is an integer) the DFT coefficients are determined using algorithm known as a fast Fourier Transform(FFT). Because of the fact that the coefficients $\hat{X}_{(N/2)+1}$ through $\hat{X}_{(N-1)}$ are complex conjugates of the coefficients $\hat{X}_1$ through $\hat{X}_{(N/2)-1}$, only the coefficients $\hat{X}_0$ through $\hat{X}_{N/2}$ are needed for the analysis of the real data.

Once the DFT coefficients are determined, the signal *x(t)* can be expressed in terms of a sum of sinusoidal components given by

$$x(t) = \frac{1}{N}\left|\hat{X}_o\right| + \frac{1}{N}\left|\hat{X}_{\frac{N}{2}}\right|.\cos(2.\pi.f_{\frac{N}{2}}.t + \Phi_{\frac{N}{2}}) + \sum_{k=1}^{\frac{N}{2}-1}\frac{2}{N}\left|\hat{X}_k\right|\cos(2.\pi.f_k.t + \Phi_k) \ , \qquad (4.3)$$

where $\hat{X}_k$, Φ_k are the amplitude the phase of *x(t)* spectrum respectively, $\Phi_k = \angle\ \hat{X}_k$. The harmonic frequencies f_k are given by $f_k = \frac{k}{T_p} = \frac{k}{N.\Delta t} = k.f$.

For the work presented here, a MATLAB program was written to implement the FFT method. In this program, the experimental data were loaded and read by MATLAB and then analyzed using an FFT. For more details about the MATLAB code used in this work see the appendix B. Once the FFT data were obtained a transfer function argument was used to interpret the behavior of the engine.

4.2 Transfer Function Analysis

A transfer function is defined as a mathematical representation of the relation between the input and the output of a linear time invariant system [30]. For a continuous- time input signal *x(t)* and output *y(t),* the transfer function is the linear mapping of the Laplace transform of the input *X(s)* , to the output *Y(s)* , given by

$$H(jw) = \frac{Y(jw)}{X(jw)} = \frac{L\big(y(t)\big)}{L\big(x(t)\big)}, \tag{4.4}$$

where *H(s)* is the transfer function of the linear system. For a discrete-time system, the transfer function *H(z)* is give by $H(z) = \frac{Y(z)}{X(z)}$, where *Y(z) and X(z)* are obtained by converting the time domain signal into complex frequency domain representation.[*Z*-transform].

The transfer function analysis was used to interpret the experimental data in the frequency domain. For the cantilever engine experiments, the fundamental time period was T_p =100 ms with fundamental frequency *f*=10.00 Hz. The duration of the pulse was *T*=10 ms. The periodic motion *x(t)* of the cover slip and the heater voltage $V_h(t)$ were recorded on a digital oscilloscope. The number of sampling points on the oscilloscope was N=2500 points. Given that the heater voltage $V_h(t)$ was periodic. The heat rate delivered to the engine given by $q(t) = \frac{V_h^2(t)}{R_h^2}$, can be represented by Fourier series as follows

$$q(t) = Q_o + \sum_{k=1}^{\frac{N}{2}-1} Q_k . \cos(2.\pi . f_k + \theta_k), \tag{4.5}$$

where Q_k and θ_k are the amplitude and the phase of the heat rate spectrum at each harmonic frequency f_k . A similar analysis was performed on the motion of the cover slip *x(t)*, i.e., amplitude X_k and phase γ_k in the Fourier series are given by

$$x(t) = X_o + \sum_{k=1}^{\frac{N}{2}-1} X_k.\cos(2.\pi.f_k + \gamma_k)\,. \tag{4.6}$$

In the measurement of the heater voltage $V_h(t)$ and the motion of the cover slip *x(t)* care was taken to insure that the sampling interval Δt used with the digital oscilloscope captured one exact period of motion so that the FFT output corresponded to the right Fourier amplitudes.

The cantilever engine performance was then interpreted using the transfer function Γ between the coefficients Q_k and X_t at frequencies f_k . According to the linear model described in sections 3.5 and 3.6, the amplitudes and phases for heat input Q_k, θ_k and motion of the cover slip X_k , γ_k , will be related by

$$X_k = \Gamma(kf_p)Q_k \ , \ \gamma_k = \theta_k + \phi(kf_p), \tag{4.7}$$

where $\Gamma(kf_p)$ and $\phi(kf_p)$ are the transfer function magnitude and phase determined from the experiment at frequencies kf_p. In this case, the heat rate *q(t),* given by (4.5) , delivered to the engine was the input to the system, while the displacement of the cover slip *x(t)*,given by (4.6) was the output from the system.

For the enclosed engine, the engine was operated at frequencies f =0.2 Hz, 4.0 Hz and 10.0 Hz respectively. The pulse duration T at each frequency f was =50, 2.5 and 1.0 ms respectively. The input to the system was the heat rate *q(t),* given by 4.5, delivered to the

engine, while the output from the system was the velocity of the upper membrane *u(t)*, given by

$$u(t)=U_0+\sum_k U_k\cos\left(2\pi kf_p+\varphi_k\right) \quad , \tag{4.8}$$

where U_k and φ_k are the amplitudes and phases of the velocity spectrum $u(t)$. The amplitudes and the phase of the upper membrane velocity are given by

$$U_k=\Gamma\left(kf_p\right)Q_k \ , \ \varphi_k=\theta_k+\varphi\left(kf_p\right) \tag{4.9}$$

where $\Gamma\left(kf_p\right)$ is the transfer function of the velocity spectrum.

4.3 Least Squares Method

The least squares method (LSM) is used to compute estimations of parameters and to fit data. The method of least squares assumes that the best fit curve for a set of data points is the one with the minimal sum of the deviations, i.e., the squares of the error, where the error measured as the difference between the measured data and model prediction.

In the least squares method, the goal is to adjust a model function to best fit the data points obtained experimentally. This is done by adjusting free parameters in the model to minimize the squares of the error. For example, let the model function is given by $Y=F(x,c)$, where Y is the dependent variable, x is the independent variable and c are the free parameters. The lease squares method minimizes the sum of the squares of the error equation described by $S=\sum_{k=1}^{k=n}(Y_i.-F(x,c))^2$, by adjusting the free parameters c, where the measured data are given by Y_i.

For the work presented here, the least squares method was used to fit the mathematical model described in sections 3.5 and 3.6 to the data points obtained experimentally. For the cantilever engine, the evaporator diameter $2r_o$, bubble diameter $2r_i$, thickness of the cavity

h , cantilever stiffness s, mass m, damping b, PF-*77* fluid properties and environment parameters, given in Table 4.1, were fixed model parameters. However, since there was no a prior estimation of the heat loss coefficient U , thermal inertia C_T , vaporization coefficient β, liquid mass $\bar{m}$, liquid damping $\bar{b}$ and evaporator stiffness s_h , those parameters were set to be free parameters used to minimize the square error between the model and measured transfer functions Γ .

For the enclosed engine a similar procedure was used to fit curve the mathematical model compared to the measured data. In this case, the fixed parameters were the evaporator diameter $2r_o$, bubble diameter $2r_i$, thickness of the cavity h , upper membrane stiffness s , lower membrane stiffness s_h , PF-*5060* fluid properties and environment parameters given in Table 4.2. Thermal losses U, the evaporation coefficient β and the viscose damping b_f were set to be the free parameters that were determined by the least squares method.

Liquid density(kg/m^3) , ρ	1780
Vapor density(kg/m^3) , ρ_o	0.55
Molecular weight(kg/mol), M	0.416
Saturated pressure(kpa) , P_o	3.13
Specific heat (J/kg.K), C_p	841
Gas constant(J /kg.K) , R	19.35
Enthalpy(J/kg), h_{fg}	93.0
$\hat{A}$	10.76
$\hat{B}$	2138
$\hat{C}$	0
To(K)	294

Table 4.1: PF-77 properties/cantilever engine configuration

Liquid density(kg/m^3) , ρ	1775
Vapor density(kg/m^3) ,ρ_o	3.53
Molecular weight(kg/mol) ,M	0.338
Saturated pressure(kpa),P_o	25.097
Specific heat (J/kg.K), C_p	755
Gas constant(J /kg.K), R	24.18
Enthalpy(J/kg) , h_{fg}	94.0
$\hat{A}$	9.73
$\hat{B}$	1562
$\hat{C}$	0

Table 4.2: PF-5060 properties/ Enclosed engine configuration

4.4 Parseval's Theorem

Parseval's theorem is often written as

$$\int_{-\infty}^{+\infty} |x(t)|^2 \, dt = \int_{-\infty}^{+\infty} \left| \hat{X}(f) \right|^2 df \,, \tag{4.10}$$

where $\hat{X}(f)$ represents the continuous Fourier transform of *x(t)* and *f* represents the frequency component. The interpretation of Parseval's theorem is that the sum of the total energy contained in a waveform *x(t)* over all the time *t* equals to the total energy of the waveform's Fourier transform $\hat{X}(f)$ summed across the continuous spectrum [30]

For a discrete Fourier transform, the relation becomes

$$\int_0^{T_P} \left(x(t) - \bar{x} \right)^2 dt = \frac{T_P}{2} \sum_{k=0}^{N-1} \left| \hat{X}_k \right|^2 \,, \tag{4.11}$$

where $\hat{X}_k$ are the discrete Fourier transform of x_n, and $\bar{x} = \frac{1}{T} \int_0^T x^2(t) dt$.

Using Parseval's theorem, a prediction of the effect of heat pulse duration on the engine performance is possible. Consider a heat rate *q*(*t*), delivered to the engine. Subject

the heat rate $q(t)$ to the constraint that there is a fixed energy E delivered to the engine per cycle, and q(t) is unipolar pulse, given by

$$q(t) = \left\{ \begin{array}{l} \overset{o}{Q}, \quad t < T \\ 0, T < t < T_p \end{array} \right\}, \tag{4.12}$$

where T is the duration of the pulse, $\overset{o}{Q}$ is the magnitude of the pulse. The energy delivered to the engine per cycle is given by $E = \overset{o}{Q} T$. The Fourier coefficients Q_k of the heat impulse given by 4.5 are then given by

$$Q_k = \frac{E}{T} \sqrt{\left[\frac{2}{k\pi} \sin\left(k\pi \frac{T}{T_p} \right) \cos\left(k\pi \frac{T}{T_p} \right) \right]^2 + \left[2 \frac{\cos^2\left(k\pi \frac{T}{T_p} \right) - 1}{k\pi} \right]^2} \quad . \quad k > 0 \tag{4.13}$$

Using Parseval's theorem, the energy delivered to the engine per cycle is rewritten in terms of E, T, T_p and given by

$$E = E\left(\frac{T}{T_p} \right)^2 + \sum_{k=1}^{\frac{N}{2}-1} \frac{T^2}{2E} Q_k^2 \quad . \tag{4.14}$$

Equation 4.14 shows that for a fixed amount of energy E delivered to the engine, the DC energy component, i.e. $E\left(\frac{T}{T_p} \right)^2$ in (4.14) depends on the ratio $\left(\frac{T}{T_p} \right)$. For example, if the ratio $\frac{T}{T_P} = 0.5$, then the DC component, $E\left(\frac{T}{T_p} \right)^2$ represents 25% of the total energy

delivered to the engine. Meanwhile, if the ratio $\frac{T}{T_P} = 0.01$, then the DC component represents only 1x 10^{-4}E. Based on this argument, a short heat rate pulse $\left(\frac{T}{T_p}\right)$ is optimal for transfer of energy to the engine. Given that a short heat rate impulse is desirable, one can determine other properties in the limit $T/T_p \to 0$. In this limit for a finite frequency bandwidth the heat rate coefficients Q_k from 4.5 become

$$\lim_{T/T_p \to 0} Q_k \approx 2 f_p E \left[1 - \left(k\pi \frac{T}{T_p} \right)^2 \right] \approx 2 f_p E \,, \qquad (4.15)$$

so in the limit $T/T_p \to 0$, the heat rate amplitudes Q_k are proportional to the fundamental frequency f_p . That means running the engine at higher frequencies is desirable. However, increasing the operating frequency f_p will place fewer components of the heat rate spectrum Q_k in the frequency bandwidth with large $\Gamma(kf_p)$.

4.5 Stiffness Measurement of the Cantilever

The stiffness of the cantilever is determined using the free vibration response and the equivalent circuit parameters obtained from the impedance information. The free vibration response of a PZT cantilever, is governed by the second order differential equation

$$m\ddot{x} + b\dot{x} + sx + \psi V = 0 \qquad (4.16)$$

where m,b,s are the equivalent mass, damping and stiffness of the cantilever respectively, ψ is the electrical-mechanical coupling factor ($N.V^{-1}$), and x is the deflection of the cantilever tip. Equation 4.16 could also be written in terms of the equivalent circuit parameters ,L,C,R , i.e.

$$L\psi^2 \ddot{x} + R\psi^2 \dot{x} + \frac{\psi^2}{C} x + \psi V = 0 \quad , \tag{4.17}$$

where L=$\frac{m}{\psi^2}$, C=$\frac{\psi^2}{s}$, R=$\frac{b}{\psi^2}$ determined from the impedance information, the pulse V is given by

$$V = \begin{cases} V_o , & t \le T \\ 0 , & t > T \end{cases}$$

where T is the pulse duration. For the derivation made here, $T << \frac{2\pi}{w_n}$, where $w_n = \frac{1}{\sqrt{LC}}$ is the resonant frequency of the cantilever.

Solving 4.16, results in

$$x(t) = \frac{I}{L w_n \sqrt{1 - C^2}} \sin\left(w_n \sqrt{1 - \xi^2 t}\right), \tag{4.18}$$

where ξ is the damping ratio, $\xi = \frac{R}{2\sqrt{L\frac{1}{C}}}$, and $I = \frac{V_o T}{\psi}$. Figure 4.1 shows the free vibration response of the cantilever, the point ($\overset{*}{x}, \overset{*}{t}$) represents the peak deflection $\overset{*}{x}$ of the cantilever at time $\overset{*}{t}$ measured experimentally. Substitute for ($\overset{*}{x}, \overset{*}{t}$) in 4.18 and simplify, results in

$$\overset{*}{x} = \frac{\left(\frac{V_o T}{\psi}\right)}{L w_n} \exp\left[\frac{-\xi}{\sqrt{1-\xi^2}} a\tan\left(\frac{\sqrt{1-\xi^2}}{\xi}\right)\right] \quad , \tag{4.19}$$

simplifying (19) and solving for ψ, results in

$$\psi = \frac{V_o T}{L w_n \overset{*}{x}} \left[1 - \left(\frac{\pi \xi}{2} \right) \right] . \tag{4.20}$$

Once ψ is determined , the stiffness of the cantilever is calculated using $s = \frac{\psi^2}{C}$.

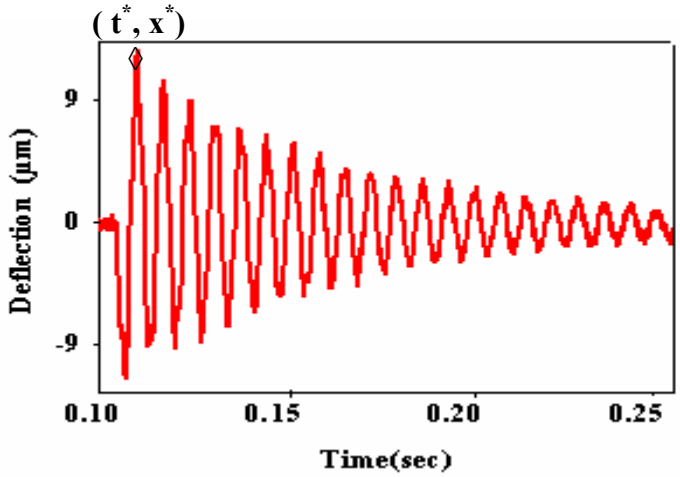

Fig. 4.1 :Free vibration response of the cantilever

4.6 Correction of the Stiffness of Silicon Nitride Membrane

In the stiffness measurement of the silicon nitride membrane described in 2.4.3, the peak deflection of the silicon nitride membrane x was measured. In the mathematical model described in 3.3-3.6, the average deflection of the silicon nitride membrane $\bar{x}$ was used to describe the stiffness of the membrane. A correlation between the peak deflection x , and the average deflection $\bar{x}$ should be established to calculate the stiffness of the membrane based on $\bar{x}$ value.

Figure 4.2 describes both, x and $\bar{x}$. In the figure, 2a is the side length of the membrane, $\bar{F}$ is the force distributed over the membrane area. The volume under the membrane , $\forall_{mem,1}$ based on the peak deflection value *x,* is determined by the equation [15]

$$\forall_{mem,1} = 16xa^2 \frac{(2R+5)}{45}, \tag{4.21}$$

where R=0.34 is a constant determined by matching the deflection profile of the equation to the experimental data. For more details on calculations of the volume under the membrane see [15].

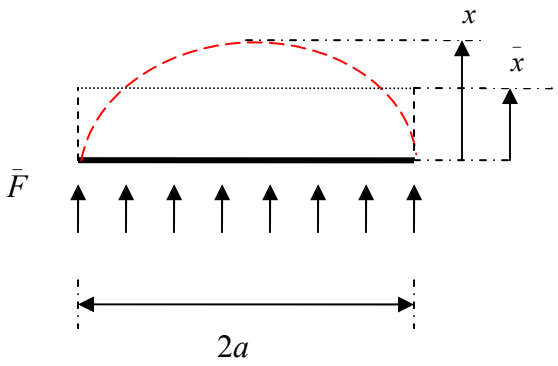

Fig. 4.2: Membrane stiffness correction

The virtual volume under the membrane based on the corrected value $\bar{x}$ is given by $\forall_{mem,2} = (2a)^2 \bar{x}$. Constrain the volume to be constant for both cases, i.e. $\forall_{mem,2} = \forall_{mem,1}$ and solving for $\bar{x}$ results in

$$\bar{x} = 0.505x, \tag{4.22}$$

assuming the stiffness of the membrane is linear. $\bar{F} = a_o x = 1.98 a_o \bar{x}$, where a_o, $1.98\,a_o$ are the stiffness of the membrane based on x and $\bar{x}$ values respectively.

For the silicon nitride membrane used in this work, the side length of the membrane was $2a$=5 mm, the stiffness of the membrane, calculated using the peak deflection x was a_o =750 N.m^{-1}, the corrected stiffness used in the model, based on $\bar{x}$,was 1485 N.m^{-1}. The pressure deflection curve of the silicon nitride membrane is shown in figure 4.3.

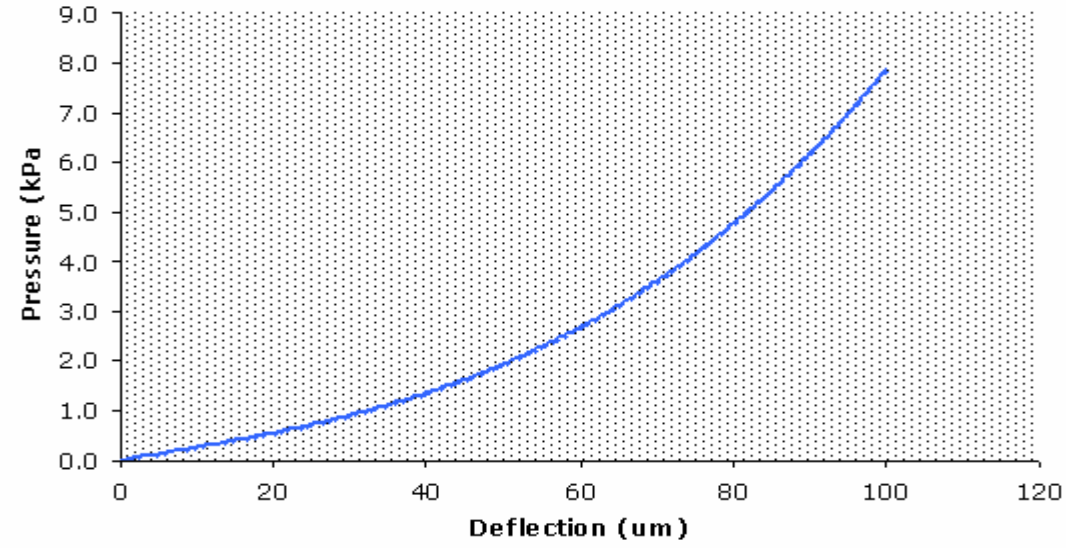

Fig. 4.3 : Pressure- deflection of silicon nitride membrane (5 mm side length)

CHAPTER 5

RESULTS

The main goal of this chapter is to address the results of the experiments carried out to understand the dynamic behavior of both the cantilever engine and the enclosed engine. Better understanding of the engine behavior will result in determination of the main parameters that affect the performance of the engine; mainly heat losses, frictional losses, evaporation efficiency, heat pulse intensity & duration, cycle frequency, and materials.

In the following sections, the assumption of the linear behavior of the engine made in chapter 3 is verified, and the mathematical model for the engine is validated experimentally. In comparing the model predictions to the experimental results, the least squares method is implemented and used to minimize the squares of the error between the model and the data obtained experimentally.

5.1 Cantilever engine configuration

5.1.1 Stiffness of the cantilever

The method described in section [4.5] was used to determine the stiffness of the cantilever. The cantilever used in this work was 40 mm in length, 18 mm wide and 600 μm thick. The cantilever was covered with PZT layers on both sides. The impedance measurements of the cantilever are shown in Figure 5.1. The resonant frequency of the cantilever was ω_n = 138.0 Hz, the electrical quality factor Q_e=45.0, and the coupling factor k^2=0.1047.

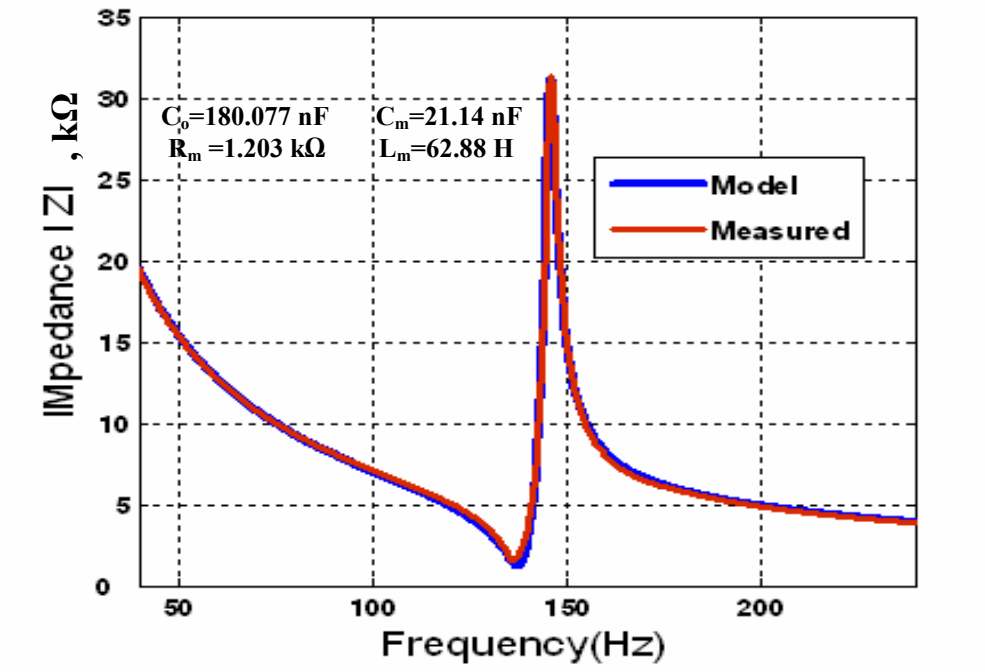

Fig .5.1: Impedance curve of the cantilever.

Once the equivalent circuit parameters were determined, the cantilever was then pulsed at 10.0 Hz for a duration of T=1.0 ms and a voltage amplitude of V_o=1.0 volt. The pulse duration T, was chosen to satisfy the condition $T << \frac{2\pi}{w_n}$. Figure 5.2 shows the free vibration response of the cantilever. The point $(\mathbf{t}^*, \mathbf{x}^*)$, shown in Figure 5.2, was used to estimate the unknown parameters of the cantilever. It was determined that the cantilever assembly had lumped parameter mass, damping , and stiffness relative to the cover-slip displacement of m=482mg, b=9.28N•s/mm, and s=362N/m respectively.

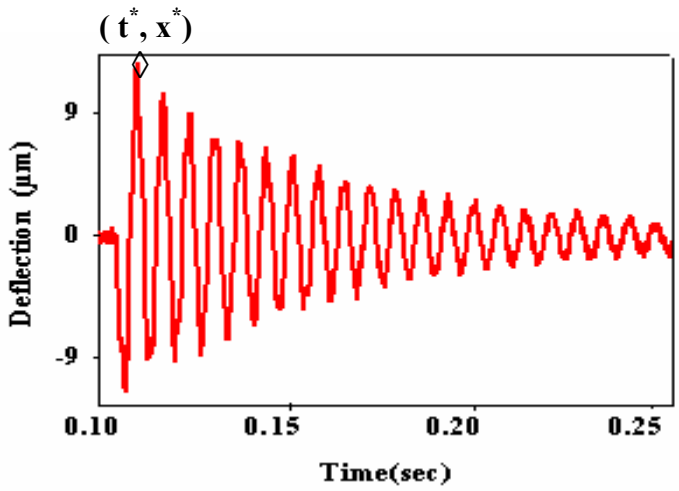

Fig .5.2: Free vibration response of the cantilever.

5.1.2 Engine Model Comparison with Experimental Measurements

Experiments were conducted for a parametric variation of bubble diameter $2r_i$ and cavity thickness h. The engine consisted of an 8.00 mm side length square lower membrane, patterned with a 300 nm thick gold heater resistance. The capillaries of the wick structure were 70 µm wide, 10 µm high and 5.00 µm thick. The cantilever had the same dimensions described in [5.1.1]. A voltage pulse was applied to the heater and the resulting deflection of the cover slip attached to the cantilever measured with the laser vibrometer. The engine was operated at f_p= 10.0 Hz with pulse duration of T=10.0 ms. Both the displacement of the cover slip and the voltage output from the cantilever were measured and recorded. Experimental cover-slip displacement amplitude transfer function X_k/Q_k and phase θ_k-γ_k , were compared to the model predictions $\Gamma(f_k)$ and $\phi(f_k)$ from (3.8, 3.19-3.21). The experimental conditions were fixed parameters in the model. The following values were used: engine diameter $2r_o$=8.00 mm, bubble diameter $2r_i$=7.2, and 4.8 mm respectively, cavity thickness h=75.0, 225.0, and 450.0 µm respectively, cantilever

stiffness s=362 N/m, mass m=482.0 mg, and damping b=9.28 N.s/mm. There was no a prior-estimate of the heat loss coefficient U, thermal inertia C_T, vaporization coefficient β, liquid mass $\overline{m}$, liquid damping coefficient $\overline{b}$, and evaporator stiffness s_h. These parameters were determined by minimizing the squares of the error between predicted and measured displacement amplitude while holding the fixed parameters constant. For more details on the least squares method used to minimize the square of the error see Appendix C.

An example for the comparison that was done between the measured transfer function and the model prediction is the case shown in figure 5.3. In Figure 5.3-a Displacement transfer function and phase versus frequency are shown. In this case, the bubble diameter was $2r_i$=7.2mm, and the thickness of the cavity was h=75μm. Experimental data are shown as square symbols and the heavy red solid line is a model prediction of cover-slip displacement amplitude transfer function Γ(f). In this comparison, the parameters U=18.8W/K, C_T=0.0 mJ/K, β=0.0029, $\overline{b}$ =0.023 Ns/m, and s_h=559 N/m were found to minimize the squares of the error between the model prediction Γ(f_k) and experimental measurements of cover-slip displacement amplitude X_k/Q_k. The agreement between experimental and modeled results is quite good. In Figure 5.3-b and c, model predictions and experimental measurements of the phase, and open circuit voltage, V_{oc} across the cantilever are plotted versus frequency. Although neither phase data nor voltage measurements were used to determine the floating parameters U, C_T, β, $\overline{m}$, $\overline{b}$, and s_h, there was favorable agreement between model prediction and experimental measurements of phase and voltage. This agreement means that the model described in [3.5] is likely a unique lumped-parameter dynamic model for the engine.

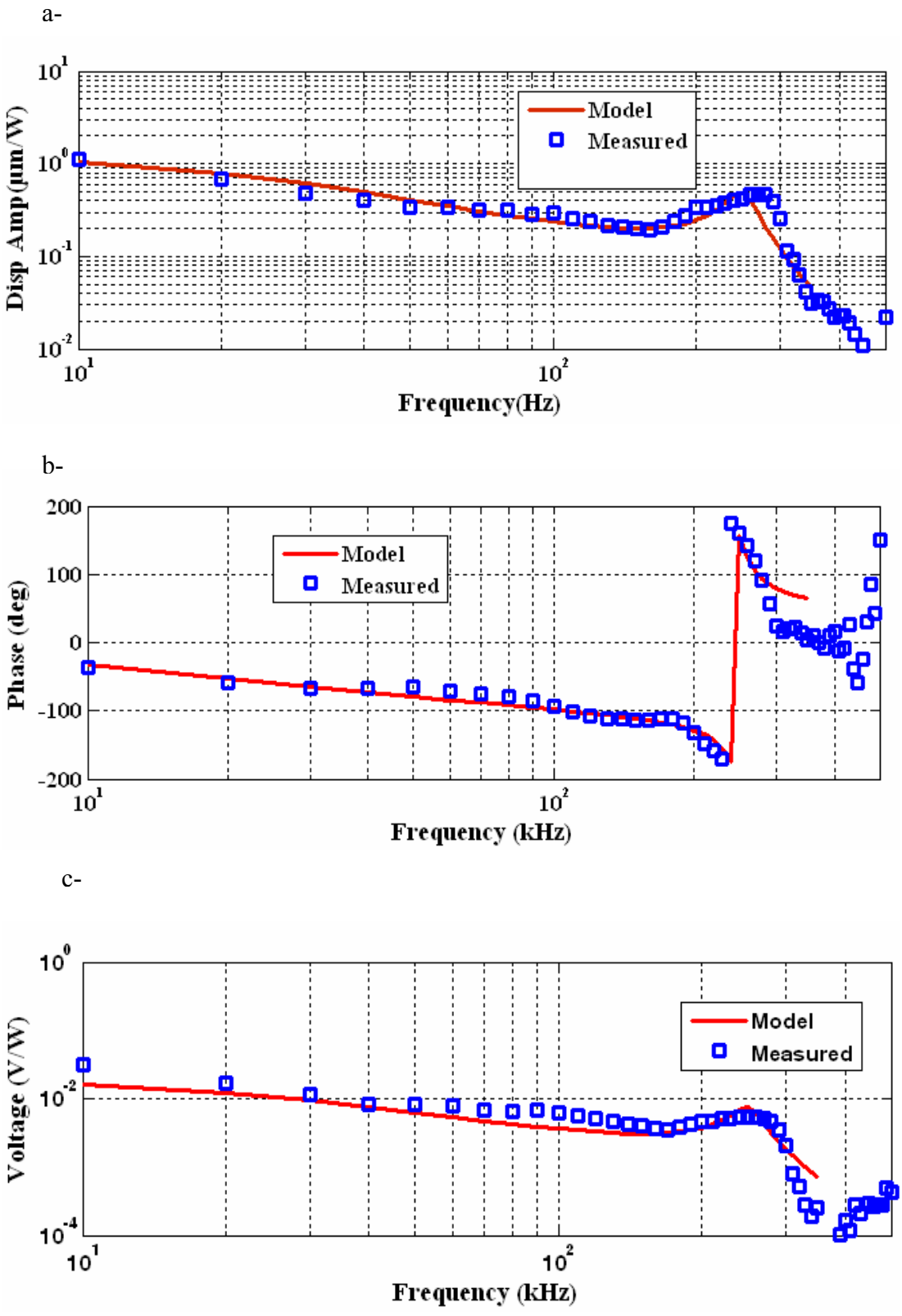

Fig. 5.3: Model & measured transfer functions. a) Displacement amplitude b) Phase c) Voltage Amplitude. Case # 3, Table 1.

5.1.3 Parametric Study

Multiple experiments were performed to investigate the performance of the engine as the thickness h and bubble size r_i were changed. In each experiment, cover-slip displacement amplitude X_k , and the output voltage amplitude V_k were measured. The least-squares procedure was then applied to determine the parameters U, C_T, β, $\overline{m}$, $\overline{b}$, and s_h for each thickness and bubble size combination. The results of these measurements and analyses are shown in Table 1. A statistical analysis of variance (ANOVA) method was used to determine trends in the parametric study.

Bubble Dia r_i (mm)	Thickness h (μm)	Heat Loss Coeff U (W/K)	Thermal Inertia C_T (mJ/K)	Vaporization Coeff β -	Liquid Mass mb (mg)	Liquid Damping bb (Ns/m)	Heater Stiffness s_h (N/m)
3.6	450	12.38	50.2	0.00960	21.70	0.06	555
3.6	225	14.1	15.6	0.00370	125.00	0.00	925
3.6	75	18.8	0.0	0.00290	0.00	0.05	559
2.4	450	48.76	0.0	0.00320	384.00	0.14	740
2.4	225	16.32	0.1	0.00420	832.00	0.00	555
2.4	75	27.07	0.0	0.01260	0.00	0.00	249

Table 1: Model parameters obtained using the least square method

The results show that, the heat loss coefficient U, ranged from 12.38-48.76W/K, was most strongly correlated to bubble diameter. An engine with smaller bubbles experienced higher heat loss. The heat loss coefficient is an indication of the portioning of the heat input. That is when heat is added to the engine, a portion of it is stored in the membrane and wick structure, a portion is conducted away to the bulk structure, a portion is conducted into the liquid, and a portion vaporizes working fluid. High values of U indicate that only a small fraction of the heat goes into evaporating liquid. The thermal inertia C_T, ranged from 0-

50.2 mJ/K, was also correlated with bubble size. An engine with thicker bubbles experienced higher thermal inertia C_T. Lastly, the vaporization coefficient β , ranged from $0.0029<\beta<0.0126$, and did not correlate with bubble size or cavity thickness.

Figure 5.4 contain displacement amplitude versus frequency for the case corresponding to the second row of Table 1. For this case the bubble diameter was $2r_i$=7.2, and the cavity thickness was h=225μm. The data show that a maximum displacement of 2.0 μm/W occurred at 10.0 Hz and then it rolled off at higher frequencies. Two lines, labeled x_{DC} and x_{f1} , are shown in Figure 5.4. The line denoted by x_{f1} represents the displacement amplitude at resonant frequency f_1, while the displacement amplitude at low frequency is denoted by x_{DC}. A resonance peak in displacement amplitude X_k was observed in Figure 5.4 at a frequency of 200 Hz . In general, an expression for the displacement amplitude x_{f1} can be derived from the model [3.6], under the assumption of C_T=0. This expression is given by

$$x_{f1} = \left(\frac{1}{\pi r_o^2}\right)\left(\frac{B}{U\rho_v}\right)\left(\frac{L}{1+C_b/C}\right)\left(\frac{1}{R+\bar{R}\left(F_{\bar{R}\bar{C}}/f_1\right)^2}\right) \tag{5.1}$$

where $F_{\bar{R}\bar{C}} = \left(\frac{1}{2\pi}\right)\left(\frac{1}{\bar{R}\bar{C}}\right)$, and $f_1 = \left(\frac{1}{2\pi}\right)\left(\frac{1}{\sqrt{L\left(\frac{\bar{C}}{1+\bar{C}/C}\right)}}\right)$,

because C_T=15.6mJ/K was small for this engine, the prediction of x_{fl} was accurate. Also, in the limit of $f \to 0$, it is possible to derive from section [3.6] the following expression for the displacement amplitude x_{DC}

$$x_{DC}(t) \approx \frac{\pi r_o^2}{s} \frac{2\gamma}{\gamma+1} \frac{\rho_o h_{fg}}{UT_o} q(t) \quad , \tag{5.2}$$

where it is assumed that $q(t)$ is slowly varying. The DC displacement amplitude x_{DC} is proportional to the area πr_o^2, latent heat h_{fg} and power input $q(t)$, while inversely proportional to the stiffness s and heat loss coefficient U. This prediction indicates that displacement at low frequency is independent of the evaporation coefficient β.

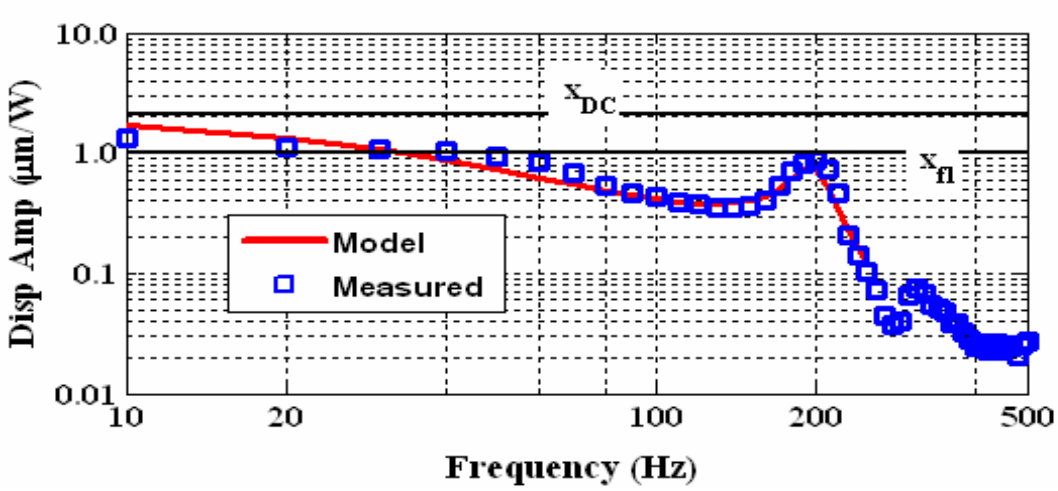

Fig. 5.4: Amplitude response. Case#2 , Table 1 .

Figures 5.5 and 5.6 contain displacement amplitude versus frequency for the cases correspond to the first and fourth rows respectively in Table 1. For these two cases the bubble diameter was $2r_i$=7.2 and 4.8 mm, while the cavity thickness was fixed at h=450μm. Case one had a relatively large thermal storage C_T =50.2 mJ/K; whereas, case

four had a small thermal storage C_T =0 mJ/K. Figure 5.5 shows that in general, the effect of large thermal storage C_T is to limit high frequency motions of the engine.

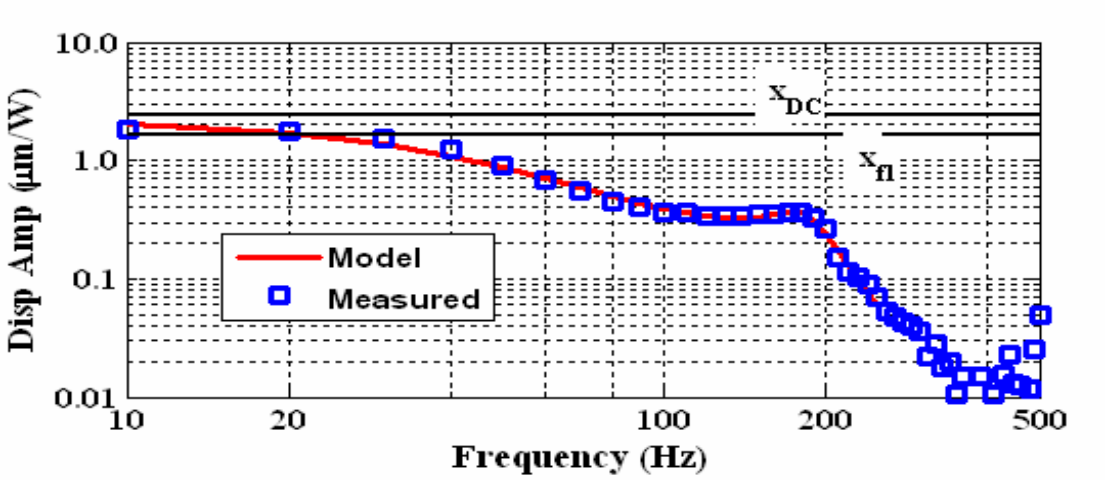

Fig. 5.5: Amplitude response for low U/high C_T. Case #1 in Table (1).

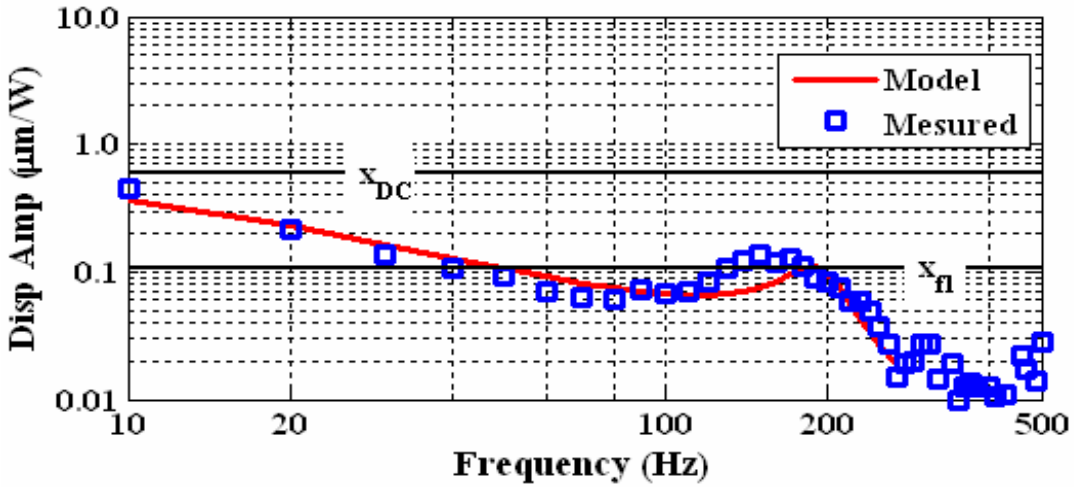

Fig. 5.6: Amplitude response high U /low C_T. Case #4 in Table (1).

Also, since the model prediction for the displacement amplitude x_{f1} at resonant frequency f_1 is made with the assumption that C_T=0, the displacement amplitude at the resonant peak f_1 was over-predicted in Figure 5.5, where C_T =50.2 mJ/K is relatively large. However, in Figure 5.6, the thermal inertia coefficient had a value of C_T=0.0mJ/K, the displacement amplitude at the peak frequency f_1 was not over-predicted.

The effect of heat loss coefficient U can be seen by comparing the low frequency displacement amplitudes in Figures 5.5 and 5.6. Case one had a relatively small heat loss coefficient U =12.38 W/K; whereas, case four had a relatively large heat loss coefficient U =48.76 W/K. In Figure 5.5, the amplitude at a frequency of 10 Hz was 2.01 μm/W, while the amplitude at a frequency of 10 Hz was 0.37 μm/W in Figure 5.6. A large value of heat loss coefficient U was associated with small low-frequency amplitude.

5.1.4 Measurement of Thermal to Electrical Efficiency

In addition to the measurement of the open circuit voltage V_{oc}, a variable load resistance R_L , was hooked up to the cantilever terminals and the voltage was measured. Later this voltage was used in electrical power and efficiency calculations. Moreover, the obtained parameters from the least squares method were used to compare the model predictions of the voltage and efficiency to the experimental data.

Figure 5.7 shows both the displacement and open circuit voltage V_{oc} transfer functions versus the frequency for the case corresponding to the fifth row in Table 1. For this case the bubble diameter was $2r_i$= 4.8 mm and the cavity thickness was h=225 μm. Once the open circuit voltage V_{oc} was obtained, the cantilever was hooked up to variable load resistance, and the voltage across the cantilever was measured.

In Figure 5.7-a and b , the measured transfer functions of both the displacement and voltage V_{oc} , are denoted by squares , while the solid lines represent the modeled transfer functions of the displacement and voltage,V_{oc} respectively. Only the displacement information was used to fit the model. The parameters obtained by minimizing the squares of the error between the model and the measured displacement data were then used to predict the transfer function of the voltage V_{oc} shown in Figure 5.7-b.

a-

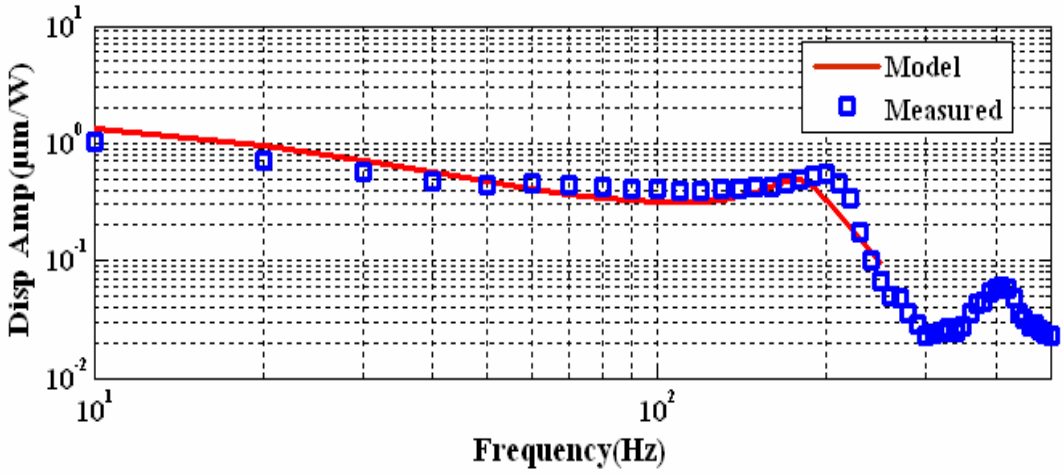

b-

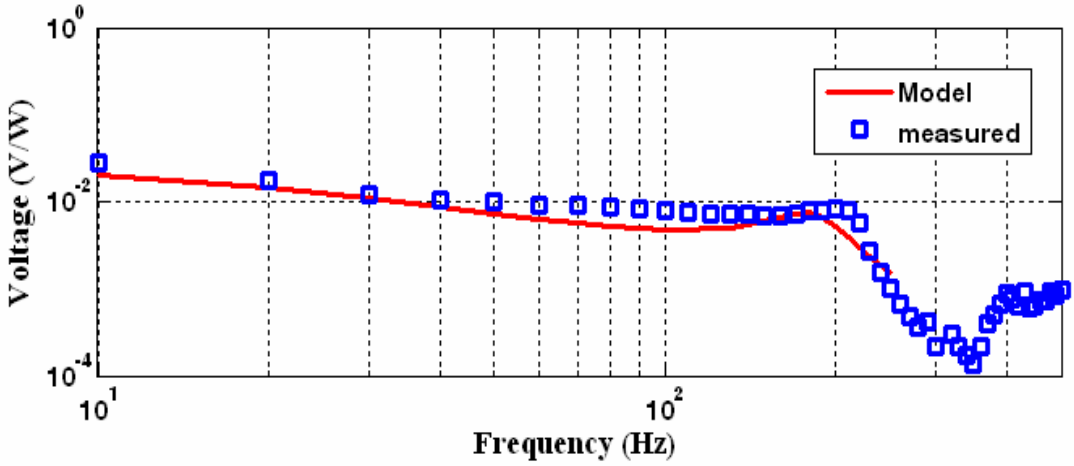

Fig.5.7: a) Displacement amplitude b) Open circuit voltage amplitude . Case # 5, Table (1).

Figure 5.8 shows the thermal to electric efficiency obtained from the experimental measurements of the voltage across different load resistances, R_L. In Figure 5.8 four different efficiency curves are shown. The values of the load resistance are, R_L =10.0 , 50,0 , 90.0 , 990.0 KΩ respectively. The data show that, a maximum thermal to electric efficiency of 2.6 x 10^{-7} % was achieved at load resistance R_L=10.0 KΩ. Efficiency decreases as the load resistance increases. Moreover, the data show that for the cases of off-the optimal load, R_L=50.0, 90.0, 990.0 KΩ, efficiency was maximum at low frequency, f=10.0 Hz, and rolled off at higher frequencies. However, for the case where the load resistance was optimum ,R_L=10.0 KΩ, the peak efficiency occurred at f = 60.0 Hz , which is lower than the displacement resonance of the engine f_p =200.0 Hz.

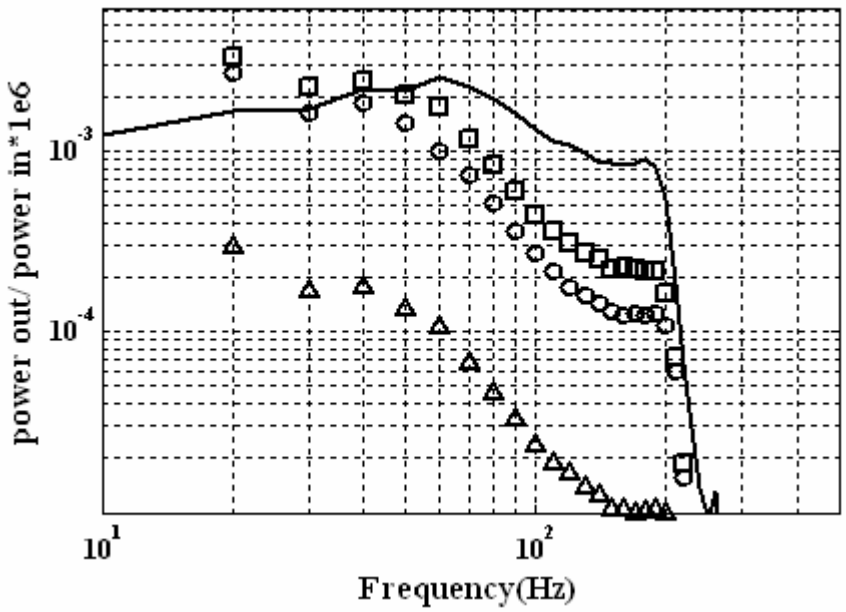

Fig. 5.8: Measured thermal to electric efficiency.

The parameters obtained from fitting the displacement transfer function shown in Figure 5.7-a were then used to predict the efficiency of the engine. Figure 5.9 shows both the efficiency calculated using the measured voltage at R_L=10.0 KΩ, and the predicted efficiency at that load. A maximum predicted efficiency of the engine, for the specified parameters, was 2.8 x 10^{-7} % compared well with the measured efficiency 2.6 x 10^{-7} %. The peak efficiency in both cases, occurred at frequency lower than the displacement resonance f_p=200 Hz. However, there was a shift in the frequency at which the peak efficiency occurred. The peak in the predicted efficiency occurred at a lower frequency, f=40.0 Hz compared to f=60.0 Hz for the measured one. Moreover, the predicted efficiency at the displacement resonant f_p was higher than the measured efficiency at that resonant. Generally speaking, the predicted efficiency had the same trend as the measured one, and a favorable agreement between the predicted efficiency and the measured efficiency was observed.

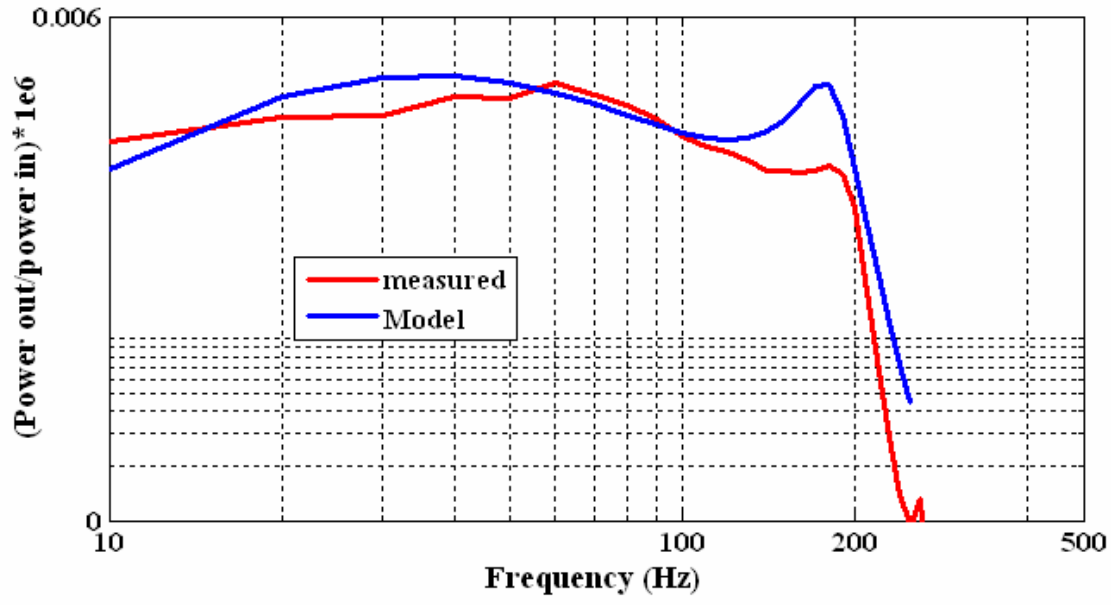

Fig. 5.9: Modeled & measured efficiency comparison at R_L=10.0 kΩ.

5.2 Enclosed Engine Configuration

In the following sections, the enclosed engine results are presented. The demonstration of the linear behavior of the engine is discussed first, next the validation of the model against the experimental data is shown, and then the effect of the heat pulse duration on the engine performance is presented.

5.2.1 Linearity Test

To demonstrate the linear behavior approximation made in [2.4.4] a separate experiment was conducted. In this experiment the input energy to the engine was varied gradually. This was done by changing the voltage amplitude V_o of the heat pulse delivered to the engine. The engine was constructed of silicon nitride upper membrane with a 5.00 mm side length, and a thickness of 2 μm. The lower membrane was a bare silicon membrane 5.00 mm on a side and 2 μm thick patterned with a 300 nm gold resistance heater. The capillaries of the wick structure patterned on the heater were 5 μm thick, 10 μm wide and 90 μm high. The cavity was 75 μm thick and was filled with PF-5060 3M working fluid. Once the engine was assembled a bubble with approximately a 4.5 mm diameter was generated. To capture the behavior of the engine over a wide range of frequencies, the engine was operated at two different cycle frequencies f_p =2.0 and 10.0 Hz. The heat pulse durations were chosen to be T = 5.0 and 1.0 ms respectively. The choice of these frequencies f_p and the pulse duration T, allowed the collection of data down to 2.0 Hz and up to 1.0 kHz. The engine was then operated and the displacement of the upper membrane X(t) was measured using the laser vibrometer. The amplitude and phase X_k , Q_k , θ_k ,and γ_k were computed from the measured displacement X(t) and the heat

rate $q(t) = \frac{V_h^2}{R_h}$ using an FFT algorithm. The transfer function $\Gamma(kf_p)$ was then computed as the ratio between the velocity amplitudes U_k and the heat rate amplitudes Q_k at frequencies f_k, i.e., $\Gamma(kf_p) = \frac{U_k}{Q_k}$.

a-

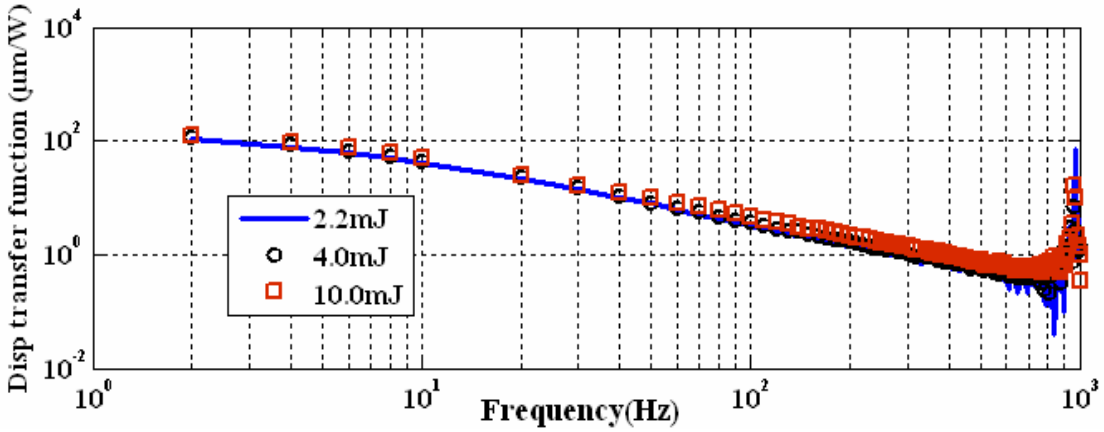

b-

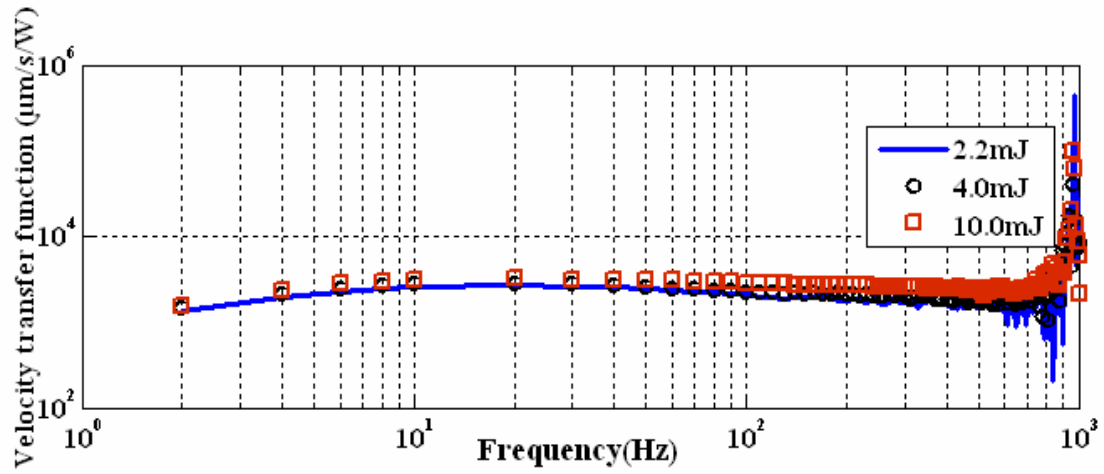

Fig. 5.10: Linearity test of the engine. a) Displacement transfer function b) velocity transfer function.

Displacement & velocity transfer functions $\Gamma(kf_p)$ versus the frequency are shown in Figure 5.9 . In the Figure, three energy levels per cycle E=2.2 ,4.0 & 10.0 mJ are shown. The data show that the energy delivered to the engine is increased by a factor of 5 , the engine behaves linearly at low frequencies. A departure from linearity starts to appear at higher frequencies, where growth in the transfer function appears for the energy levels E=4.2 &10.0 mJ. However, the observed nonlinear behavior of the engine at higher frequencies is quite small and does not appear to compromise the overall success of the model.

5.2.2 Validation of the Model

In the experiment conducted to validate the model, the same engine specifications described in [5.2.1] were used. To capture the roll-off frequencies f1 & f2, shown in Figure 5.10, the engine was operated at cycle frequencies, f_p = 0.1, 1.0, 10.0 Hz respectively. The heat pulse durations were chosen to be, T= 100 , 10 , and 1.0 ms for each cycle frequency, respectively. The choice of frequencies f_p and pulse duration T, allowed data collection down to 0.1 Hz and up to 1.0 kHz. Over all the experiments, the input energy per cycle was held constant at E=11.0 mJ. Holding the input energy per cycle constant over the experiments is important in later steps. That is, when the data collected at each cycle frequency f_p are combined together for the purpose of FFT analysis.

The engine was then operated, and the displacement of the upper membrane X(t) was measured using the laser vibrometer. The collected data at each cycle frequency; i.e f_p = 0.1, 1.0, 10.0 were then combined together and an FFT algorithm was used to decompose the displacement X(t), the velocity of the upper membrane $u(t)$,and the heat rate pulse q(t) into their amplitudes and phases X_k , U_k , Q_k , θ_k , φ_k and γ_k respectively . The use of the

FFT analysis allows the direct comparison between the measured data and the modeled one. Experimental measurements of the transfer function $\Gamma(kf_p)$ for the engine are shown in Figure 5.10. Experimental measurements are indicated by the squares while the predictions are shown with solid line. For the engine tested here, the model parameters were the engine side length $2r_o$=5 mm, the thickness of the cavity h = 75 μm, the radius of the bubble $2r_i$ = 4.5 mm, the vapor density ρo =3.53 kg/m^3, the specific heat of the working fluid c_p=7552 J/kg.K and c_v=731 J/kg•K , the saturated pressure P_o =25.097 kPa, the enthalpy h_{fg} =94 kJ/kg, Antoine parameters $A = \hat{9}.73, B = \hat{1}562, \hat{C} = 0$, the molecular weight M =0.338 kg/mol ,the upper membrane stiffness, s= 1485 N/m , the ambient temperature T_o=25 ^oC , and the lower membrane stiffness s_h=2475 N/m . Since the experimentally measured transfer function Γ showed no resonant frequency peak below 2.00 KHz, the effective mass of the engine was set $m + \bar{m} = 0$. Since there was no prior estimation for the thermal losses U, the evaporation coefficient β, and the viscous damping b_f, the least squares procedure was used to determine their values. Values of U=0.0034 kJ/kg.K, β=0.0003, and b_f =1.43 N.s/m were found to minimize the squares of the error. A quite good agreement between the model prediction and the experimental data is seen there, in spite of the fact that only three free parameters were used to minimize the square of the error. For more details on the least squares method used to minimize the square of the error see Appendix D.

a-

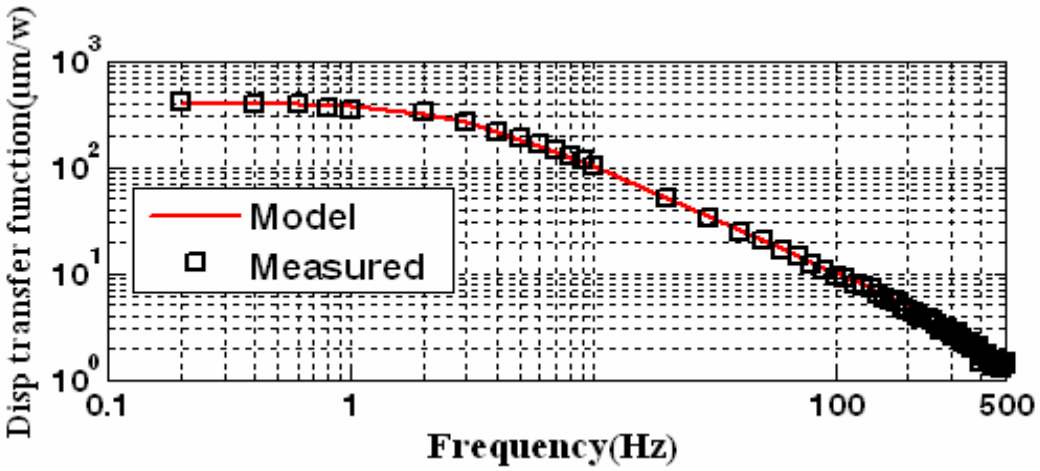

b-

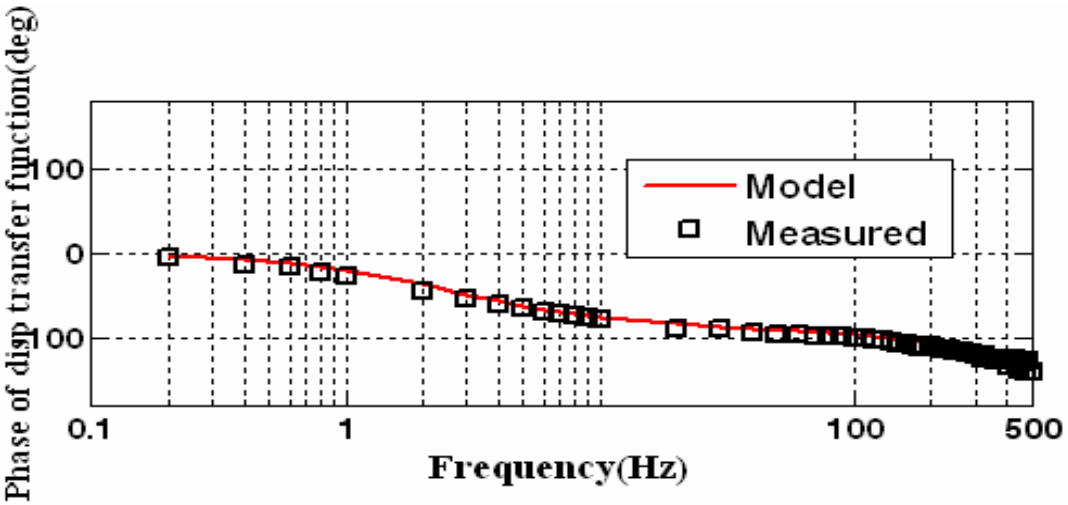

c-

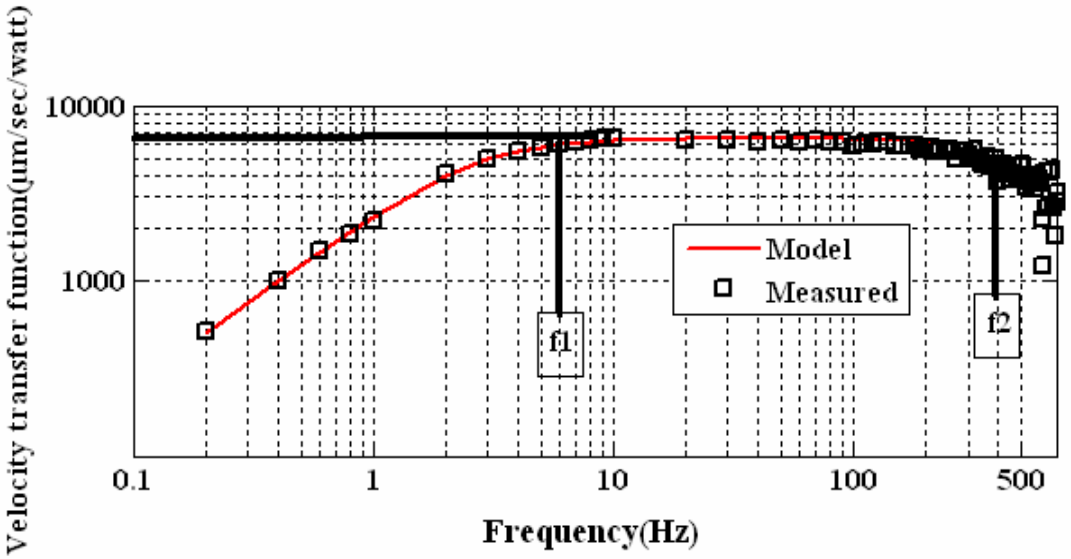

Fig. 5.10 : Model Vs measured data a)-Displacement transfer function b)-phase of the displacement transfer function c)-Velocity transfer function.

In general, the transfer function Γ is a band pass filter, consistting of successive high -and low pass sections. The high pass frequency f1= 6.0 Hz, the low pass frequency f2=400.00 Hz and the band pass amplitude Γ́=7.0 mm/s/Watt are denoted by solid lines in the figure. The value of f1 is set by the thermal losses U and the evaporation coefficient β. The total damping $b+b_f$ sets the value of f2. For the best performance, Q_k should fall between f1 and f2. The low-and high pass cut-off frequencies f1, f2 are given by

$$f_1 = \left(\frac{1}{C\,\bar{R}}\right)\left(\frac{1+\left(1+\frac{\bar{C}}{C}\right)\frac{\bar{C}}{C}}{2\left(1+\frac{\bar{C}}{C}\right)}\right) \qquad f_2 = \left(\frac{1}{R\,\bar{C}}\right)\left(\frac{1+\frac{R}{\bar{R}}\frac{\bar{C}}{C}}{1+\frac{R}{\bar{R}}+\frac{\bar{C}}{C}}\right).$$

5.2.3 Heat Pulse duration

The heat pulse duration has a major effect on the performance of the engine. To examine this factor, an engine with the same specifications described in [5.2.1] was operated at cycle frequency f_p=10.0 Hz. The engine then was pulsed for duration of T=1.00 ms , and 50.00 ms respectively. The energy per cycle delivered to the engine was kept constant in both cases to allow for direct comparison, E=7.5 mJ. Both the displacement of the upper membrane X(t), and the input heat delivered to the engine q(t) were recorded and then decomposed using the transfer function analysis described in [4.3]. Figure 5.11-a shows the heat rate amplitudes Q_k for pulse durations of T=1.00, and 50.00 ms. For a pulse duration of T=50ms, there were nonzero heat rate components Q_k at odd multiples of the engine cycle frequency, the largest occurring at a frequency f_1=10Hz of amplitude Q_1=10.6E. The amplitude of the components Q_k declined rapidly as frequency increased.

For a pulse duration of T=1.00 ms, the amplitude of the first heat rate component was Q_1=20E, and the components at higher frequencies declined very little. This value obtained for Q1 compares well with the value obtained using Parseval's theorem. That is for a short heat rate impulse, i.e. limit $T/T_p \to 0$, the heat rate coefficients Q_k are given by

$$\lim_{T/T_p \to 0} Q_k \approx 2 f_p E \left[1 - \left(k\pi \frac{T}{T_p} \right)^2 \right] \approx 2 f_p E ,$$

For f_p=10.0 Hz, and T/T_p =0.01. The calculated value of Q_1 =20E is the same as the measured value.

Figure 5.11-b shows the velocity components U_k, of the upper membrane at 1.00 ms and 50.00 ms. The data show that, a maximum velocity of the upper membrane, u= 700 μm/s happened when the engine was operated at f_p=10.0 Hz and pulsed at 1.00 ms compared to a maximum velocity of 400 μm/s when the engine was operated at 10.0 Hz and pulsed for 50.0 ms. Also, for the case where the engine was pulsed for 50.0 ms, the data show that the amplitude of the velocity components U_k declined rapidly as frequency increased.

a -

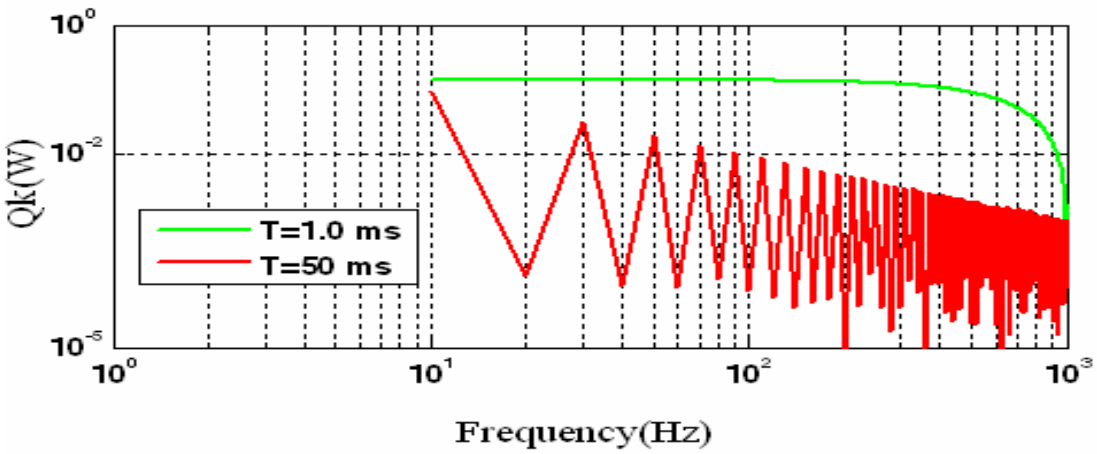

b

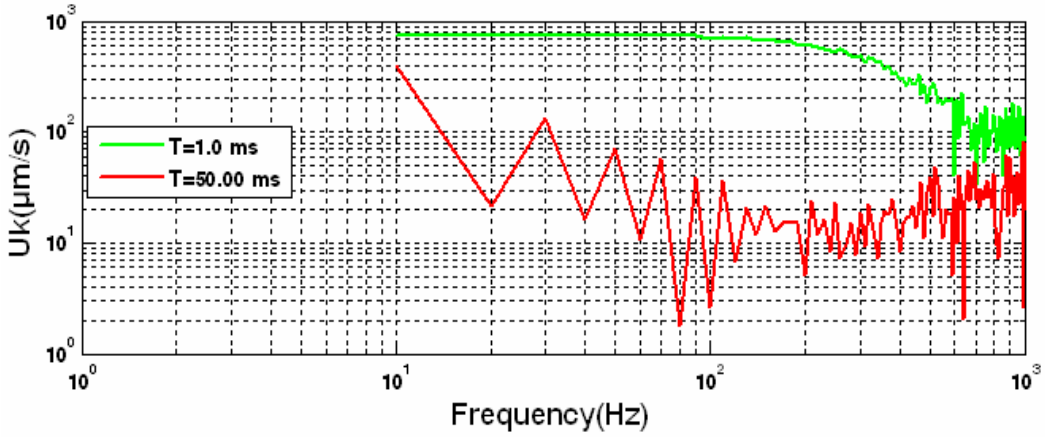

Fig. 5.11: a)-Heat pulse spectrum b)- Velocity Spectrum.

CHAPTER 6

CONCLUSIONS

A lumped parameter model was developed to capture the dynamic behavior of a micro heat engine, thus predicting the forces and displacements produced by addition of the heat to the engine. Newton's second law, conservation of energy, and mass and heat transfer equations were used to develop the model. The model was validated experimentally against two different engines; the enclosed, and the cantilever engines. A favorable agreement between the model predictions and the experimental results was observed.

The results of the cantilever engine showed that the displacement of the cantilever was maximized for low frequency operation. As the frequency increased, the displacement decreased. A resonant peak in the displacement occurred at f_p=200.0 Hz. For the cases reported here, the amplitude of the resonant peak was always less than the amplitude of the displacement obtained at low frequency operation.

A parametric study was performed to investigate the performance of the cantilever engine as the thickness h and bubble size r_i were changed. The results showed that the heat loss coefficient U, was most strongly correlated to bubble diameter. An engine with smaller bubbles experienced higher heat loss. Moreover, the thermal inertia C_T was also correlated with bubble size. An engine with bigger bubbles showed higher thermal inertia C_T. However, the vaporization coefficient β did not correlate with bubble size or cavity thickness. The model predicts that increasing the area or decreasing the stiffness of the actuator will increase the displacement at low frequencies. The model also predicts that

small values of the heat loss coefficient, U will increase the displacement amplitude at low frequency.

In addition to the displacement measurements, the voltage across the cantilever terminals was measured at different load resistances R_L, and then used to estimate the thermal to electric efficiency at those load resistances. A maximum efficiency of 2.6×10^{-7} % was achieved at load resistance R_L=10.0 KΩ. In those measurements, although only the displacement data were used to minimize the squares of the errors, thus determining the free parameters in the model, a good agreement between the predicted voltage and the measured one was observed. In conclusion, the cantilever engine was associated with large values of heat loss coefficients and low thermal-electrical efficiency.

As a next step, an enclosed engine was examined. The enclosed engine showed a linear behavior over a wide range of frequencies, up to 100 Hz. However, as the input energy to the engine increased, a departure from linearity started to appear at higher frequencies.

The model was then validated against the experimental results. The parameters, found to minimize the squares of the error between the model prediction and the measured data were the vaporization coefficient β =0.0003, frictional damping b_f=1.43 N.s/m, and heat loss coefficient U=0.034 kJ/kg.K. Since the measured data showed no resonant peak in displacement up to 2.0 kHz , the effective mass of the engine was set $m + \bar{m} = 0$. The results from the velocity transfer function showed that, In general, the transfer function Γ is a band pass filter, consisted of successive high -and low pass sections. The high pass frequency f1, is set by the thermal losses U and the evaporation coefficient β, while the

total damping $b+b_f$ sets the value of the low pass frequency,f2. For the best performance, the heat rate amplitudes Q_k should fall between f1 and f2.

The effect of the heat pulse duration,T on the engine performance was examined. The results showed that, the amplitude of the velocity components U_k was maximized for the shorter heat pulse. Moreover, the amplitude of the velocity components U_k declined rapidly as frequency increased for the longer heat pulse duration. In conclusion, short pulse duration is desirable, because the heat rate amplitudes Q_k have larger values over a wider frequency spectrum.

Reference:

1. P., Bergstrom, J., Ji, Y., Liu, M., Kaviany, K., Wise, "Thermally Driven Phase-Change Microactuation", Journal of Microelectromechanical Systems, Vol. 4, no. 2, pp. 10-17, 1995.
2. L., Lagorce, O., Brand, M., Allen, "Magnetic Microactuators Based on Polymer Magnets", Journal of Microelectromechanical Systems, Vol. 8, no.1, pp. 2-9, March, 2003.
3. J., Grade, H., Jerman, MEMS Electrostatic Actuators for Optical Switching Applications, Iolon ,Inc, 2000.
4. D., Fuffieux, M.,Dubois, N.F., de Rooji , "An ALN Piezoelectric Microactautor Array".
5. D., Popa, B., Hun Kang, J., Wen, "Dynamic Modeling and Input Shaping of Thermal Bimorph MEMS Actuators", Proceeding of the 2003 IEEE International Conference on Robotics & Automation, Taipei, Taiwan, pp. 1470-1475 , 2003.
6. H., Takao, *et al,* "A Thermo-Pneumatic Microvalve with PDMS Diaphragm for Integrated Blood Examination System on Silicon ", ", proceeding of the 12th International Conference on Solid State Sensors , Actuators and Microsystems, Boston , June 8-12 , Vol.4, pp.139-142 , 2003.
7. S. Whalen, C. Richards, D. Bahr, R. Richards, "Characterization and modeling of a microcapilary driven liquid-vapor phase-change membrane actuator," Sensors and Actuators A Physical, Vol. 134, pp. 201 – 212, 2007.
8. G., Schabmueller, C., Niblock, T., "Time Constant and Lateral Resonances of Thermal Vertical Bimorph Actuators", Journal of Micromechanics and Microengineering, Vol. 12, pp. 410-413, 2002.

9. L., Fan, Y.-C. Tao, R., Muller, " IC- Processed Electrostatic Micromotors" , IEEE International Electronic Devices Meeting, 1988

10. P., Basset, A., Kaiser, P., Bigotte, D., Collard, L., Buchaillot, "A Large Stepwise Motion Electrostatic Actuator for a Wireless Microrobot", proceedings of IEEE Micro Electro Mechanical Systems, Las Vegas, NV, pp. 606-609, Jan., 2002.

11. K., Uchino, K., Ohnishi, Linear motor, U.S.patent Number 4,857,791,7 Claims , Assignee: Nissan MOTOR Co.Ltd., YoKohama ,Japan Alps Electric Co.Ltd ., Tokyo, Japan ,15 August 1989.

12. J.,Friend, J., Satonobu, K., Nakamura, S., Ueha, D., Stutts, " A single Elelment Piezoelectric Tuning Fork Linear Actuator " , IEEE Trans. Ultrason. Ferroelectric. Freq. Control 50 (2) (2003) (179-186).

13. J., Friend, A., Umeshima, T., Ishii, K., Nakamura, S., Ueha, "A Piezoelectric linear Actuator Formed from a Multitude of Bimorphs", Sensors and Actuators A, Vol. 109, pp. 242-251, 2004.

14. Liu, Chang, Foundation of MEMS, Pearson Education, Inc., New Jersey. 2006

15. S.,Whalen, Cycle Work from A MEMS Heat Engine and Characterization of the Liquid-Vapor Phase Change A actuation mechanism. Ph.D. Dissertation, WSU Mechanical and Material Engineering Department, 2004.

16. A., Wego, H., Glock, L., Pagel, S., Richter, "Investigation on Thermo-Pneumatic Volume Actuators Based on PCB Technology", Sensors and Actuators A, Vol. 93, pp. 95-102, 2001.

17. J., Abadie, N., Chaillet, C., Lexcellence, “An Integrated Shape Memory Alloy Micro-Actuator Controlled by Thermoelectric Effect”, Sensors and Actuators A, Vol. 99, pp. 297-303, 2002.

18. E., Carlen, C., Mastrangelo, “Electrothermally Activated Paraffin Microactuators”, Journal of Microelectromechanical Systems, Vol. 11, no. 3, pp. 165-174, June, 2002.

19. A., Henning, “Comprehensive Model for Thermopneumatic Actuator and Microvalves”, Journal of Microelectromechanical Systems, Vol. 15, no. 5, October 2006.

20. L., Lin, A., Pisano, “Thermal Bubble Powered Microactuators”, Microsystem Technologies, Vol. 1, pp. 51-58, 1994.

21. K., Fu, A., Knobloch, F., Martinez, D., Walther, C., Fernandez, A., Pisano, D., Liepmann “Design and Fabrication of A Silicon- Based MEMS Rotary Engine”, proceeding of ASME International Mechanical Engineering Congress and Exposition, New York, November ,2001.

22. Epstein, A., et al., “Power MEMS and Microengines”, Proceedings of Transducers '97: 1997 International Conference on Solid-State Sensors and Actuators, Chicago, Il, June, pp. 753-756, 1997

23. 23- Ravi Khanna, “MEMS fabrication perspectives from the MIT microengine project”, Surface and Coatings Technology, pp. 163-164, 2003.

24- Jeong, Cho ., Electro-Mechanical Characterization of piezoelectrics for MEMS Power, M.S. Thesis, WSU, Department of Mechanical Engineering, p.40-54; 2004

25- Vibrometer Controller OFV-5000, Polytec.

26- Agilent 4294A Precision Impedance Analyzer Operation Manual, Agilent Technologies, 2003.

27- R. W. Schrage, A Theoretical Study of Interphase Mass Transfer , Columbia, 1953

28- Y.A.Cengel, M.A.Boles, Thermodynamics An Engineering Approach , Mc Qraw Hill, 5th Edition pp111-159 , 2005.

29- Abdi, H. Least-squares, M. Lewis-Beck, A. Bryman, T. Futing (Eds*):* Encyclopedia. for research methods for the social sciences. Thousand Oaks (CA): pp. 792-795.

30- http:// http://wikipedia.org/wiki/Least_squares.

APPENDIX A

SOLUTION OF THE LINEAR SYSTEM OF EQUATIONS

For the linear system of equations described in section 3.5, a state space representation of the six equations is given by:

$$[A]\left\{\dot{X}\right\} = [B]\{X\} + \{C\}q(t) \quad , \tag{1}$$

where

$$\left\{\dot{X}\right\} = \begin{Bmatrix} \Delta \dot{V}_g \\ \Delta \ddot{V}_g \\ \Delta \dot{p} \\ \Delta \dot{T} \\ \frac{\psi}{\pi r_o^{\,2}} \dot{V} \\ \Delta \dot{T}_l \end{Bmatrix} \quad , \quad \{X\} = \begin{Bmatrix} \Delta V_g \\ \Delta \dot{V}_g \\ \Delta p \\ \Delta T \\ \frac{\psi}{\pi r_o^{\,2}} V \\ \Delta T_l \end{Bmatrix}$$

$$A=\begin{bmatrix} 1 & 0 & 0 & 0 & 0 & 0 \\ 0 & \frac{(m+\bar{m})}{(\pi r_o^2)^2} & 0 & 0 & 0 & 0 \\ 1 & 0 & \frac{(\pi r_o^2)}{S_h}+\frac{V_o}{\rho_o R T_o} & \frac{V_o}{T_o} & 0 & 0 \\ 0 & 0 & -\frac{V_o}{\rho_o C_p T_o} & \frac{V_o}{T_o} & 0 & 0 \\ -1 & 0 & 0 & 0 & \frac{(\pi r_o^2)^2}{\psi^2} C_o & 0 \\ 0 & 0 & 0 & 0 & 0 & \frac{C_T}{\rho_o h_{fg}} \end{bmatrix}$$

$$
B=\begin{bmatrix}
0 & 1 & 0 & 0 & 0 & 0 \\
\dfrac{S}{(\pi\, r_o^2)^2} & \dfrac{(b+\bar{b})}{(\pi r_o^2)^2} & -1 & 0 & 1 & 0 \\
0 & 1 & \dfrac{\bar{\beta}}{\rho_o}\sqrt{\dfrac{M}{2\pi R_u}}\dfrac{1}{\sqrt{T_o}} & -\dfrac{\bar{\beta}}{\rho_o}\sqrt{\dfrac{M}{2\pi R_u}}\dfrac{\bar{\rho}R}{2\sqrt{T_o}} & 0 & -B \\
0 & 0 & 0 & \dfrac{U}{T_o c_p \rho_o} & 0 & 0 \\
0 & -1 & 0 & 0 & \dfrac{-1}{\dfrac{\psi^2}{(\pi r_o^2)^2}R_L} & 0 \\
0 & 0 & -\dfrac{\bar{\beta}}{\rho_o}\sqrt{\dfrac{M}{2\pi R_u}}\dfrac{1}{\sqrt{T_o}} & \dfrac{\bar{\beta}}{\rho_o}\sqrt{\dfrac{M}{2\pi R_u}}\dfrac{R\bar{\rho}}{2\sqrt{T_o}} & 0 & \dfrac{B}{\rho_o}
\end{bmatrix}
$$

$$C = \begin{bmatrix} 0 \\ 0 \\ 0 \\ 0 \\ 0 \\ 0 \\ \dfrac{1}{\left(\dfrac{U}{h_{fg} B} + 1\right) \rho_o \bullet h_{fg}} \end{bmatrix}.$$

Assume the solution to be in the form

$$X_i = \hat{X}_i \, e^{j\omega t} \quad , \tag{2}$$

then

$$\dot{X} = j\omega \left\{ \hat{X} \right\} e^{j\omega t} \, , \tag{3}$$

substitute (2) and (3) in (1) and solve for the unknown $\hat{X}$ results in

$$\left\{ \hat{X} \right\} = \left[j\omega \, [A] - [B] \right]^{-1} \{C\}, \tag{4}$$

then

$$\{X(t)\} = \mathrm{Re}\left[\hat{X}\exp(jwt)\right] = \left\{\left|\hat{X}\right|\cos(wt+\phi)\right\}, \tag{5}$$

where $\phi = \angle \hat{X}$.

APPENDIX B

MATLAB CODE FOR FFT ANALYSIS OF THE MEASURED DATA

```
%FFT Analysis of the measured data and transfer function analysis.
%Input to the system is the heat delivered to the engine.
%Output from the system is the deflection of the cantilever
%====================================
clear all
close all
clc
%====================================
load m5u.txt -ascii                  ; %LOADING THE DATA FILE TO BE READ
BY MATLAB.
x=m5u(:,7)                           ; %STORE THE 7th COL IN THE IMPUT
FILE AS VARIABLE "X".
t=m5u(:,1)                           ;
N=2500                               ; %N IS THE NUMBER OF TH SAMPLING
POINTS.
dt=t(2)-t(1)                         ;
fs=1/dt                              ;
fn=fs/2                              ;
y1=fft(x)                            ;
y1=y1(1:(N/2)+1)                     ;
m1=abs(y1)                           ;
p1=angle(y1)*(180/pi)                ;
m1=(2/N)*m1                          ;
f=linspace(0,fn,(N/2)+1)             ;
%====================================
v=m5u(:,6)                           ;
v1=21.2-v                            ; %STORE THE VOLTAGE ACROSS THE
HEATER AS VARIABLE "V1".
R1=8.0                               ;
y2=fft(v1.^2/(R1))                   ;
y2=y2(1:(N/2)+1)                     ;
m2=abs(y2)                           ;
m2=(2/N)*m2                          ;
p2=angle(y2)*(180/pi)                ;
f=linspace(0,fn,(N/2)+1)             ;
%====================================
x3=m5u(:,2)                          ;
y3=fft(x3)                           ;
y3=y3(1:(N/2)+1)                     ;
m3=abs(y3)                           ;
p3=angle(y3)*(180/pi)                ;
m3=(2/N)*m3                          ;
f=linspace(0,fn,(N/2)+1)             ;
g=angle(y1./y2)*(180/pi)             ; %g is the phase of the transfer
function of the cantilever
g=angle(y3./y2)*(180/pi)             ;
%====================================
figure
subplot(2,1,1)
```

```
loglog(f',m1./m2,'r')
grid on
ylabel('Y1/Y2')
xlabel('Frequency(Hz)')
title('Displacement Transfer function of the cantilever')
%
subplot(2,1,2)
semilogx(f',g,'y')
grid on
xlabel('Frequency(Hz)')
ylabel('angel(Y1./Y2)*180/pi')
title('Phase spectrum of the displacement transfer function of the
cantilever ')
%
figure
subplot(2,1,1)
loglog(f',m3./m2,'r')
grid on;
ylabel('Y3./Y2')
xlabel('Frequency(Hz)')
title('Voltage Transfer function of the cantilever')
%
subplot(2,1,2)
semilogx(f,g,'m')
grid on;
xlabel('frequency(Hz)')
ylabel('angel(Y3./Y2)*180/pi')
title('Phase spectrum of the voltage transfer function of the
cantilever')
%==================================
```

APPENDIX C

MATLAB CODE FOR LEAST SQUARE METHOD (CANTELEVER CONFIGURATION)

```
%THIS FILE STORES THE DEFAULT PARAMETERS OF THE CANTILEVER
ENGINE,INCLUDING FC-77
%WROKING FLUID PROPETIES
%=========================================
clear all;
close all;
clc      ;
%=========================================
% Properties of the fluid
P.rhov=0.55                          ;
P.rhol=1780                          ;
P.mul=1.3e-3                         ;
P.M=416/1000                         ;
P.Ru=8.31                            ;
P.Ah=10.768                          ;
P.Bh=2138.9                          ;
P.Ch=0                               ;
P.cp=841                             ;
Psat=3.13                            ;
P.R=(Psat*1000)/(P.rhov*(273+21));
P.cv=P.cp-P.R                        ;
P.g=P.cp/P.cv                        ;
P.hfg=98.381e03                      ;
%=========================================
% Properties of the engine
P.Q=45                           ;
P.fn=138                         ;
P.s=362                          ;
P.m=P.s/((2*pi*P.fn)^2)          ;
P.b=sqrt(P.m*P.s)/P.Q            ;
P.Co=1.8077e-7                   ;
P.psi=2.77e-3                    ;
P.ro=(8e-3)/2                    ;
P.ri=(9/10)*P.ro                 ;
P.L=75e-6                        ;
P.S=pi*P.ri^2                    ;
P.Vo=P.S*P.L                     ;
P.beta=0.5                       ;
P.betab=P.beta*P.S               ;
P.sh=1*P.s                       ;
P.CT=1e-1                        ;
P.hB=1e-6                        ;
%=========================================
%  Environmental parameters
P.To=294                             ;
P.Po=10^(P.Ah-(P.Bh/(P.To+P.Ch)));
%=========================================
```

```
%  Computed parameters
P.B=P.betab*sqrt(P.M/(2*pi*P.Ru))                                          ;
P.B=P.B*(10^(P.Ah-(P.Bh/(P.To+P.Ch))))/sqrt(P.To)                          ;
P.B=P.B*( ((P.Bh*log(10))/(P.To+P.Ch)^2)-(1/(2*P.To)) )                    ;
P.U=1*P.B*P.hfg                                                            ;
P.wo=2*pi*100                                                              ;
P.lv=sqrt((2*P.mul)/(P.wo*P.rhol))                                         ;
P.al=pi*(P.ro^4)*( log(P.ro/P.ri)-(1/4)*(3-(P.ri/P.ro)^2)*(1-
(P.ri/P.ro)^2) )                                                           ;
P.mb=(P.rhol/(2*P.L))*(1+(P.lv/P.L))*P.al                                  ;
P.mb=P.mb*1                                                                ;
P.bb=((P.rhol*P.wo)/(2*P.L))*((P.lv/P.L)*P.al)                             ;
P.fn=(1/(2*pi))*sqrt(P.s/(P.m+P.mb))                                       ;
P.Cob=((pi*P.ro^2)^2/P.psi^2)*P.Co                                         ;
P.RL=1/(2*pi*P.fn*P.Co)                                                    ;
P.RL=P.RL*1e6                                                              ;
% Mag factor for RL
P.RLb=(P.psi^2/(pi*P.ro^2)^2)*P.RL                                         ;
P.Rb=(P.U/P.hfg)/((P.U/P.hfg)+P.B)                                         ;
P.Rb=P.Rb*(P.betab/P.rhov)*sqrt(P.M/(2*pi*P.Ru))*(P.g+1)/(2*P.g*sqrt(P.To
))                                                                         ;
P.Rb=1/P.Rb                                                                ;
P.Cb=(P.Vo/(P.g*P.rhov*P.R*P.To))+(((pi*P.ri^2)^2)/P.sh)                   ;
P.fRbCb=(1/(2*pi))*(1/(P.Rb*P.Cb))                                         ;
P.R1=(P.b+P.bb)/((pi*P.ro^2)^2)                                            ;
P.C1=((pi*P.ro^2)^2)/P.s                                                   ;
P.L1=(P.m+P.mb)/((pi*P.ro^2)^2)                                            ;
P.f1=P.Cb/(1+(P.Cb/P.C1))                                                  ;
P.f1=(1/(2*pi))*sqrt(1/(P.f1*P.L1))                                        ;
P.fRbR=(P.Rb)/((P.b+P.bb)/(pi*P.ro^2)^2)                                   ;
P.CbC=(P.Cb)/(((pi*P.ro^2)^2)/P.sh)                                        ;
```

```
%=========================================
%THIS SUBROTUINE IS USED TO CONSTRUCT THE MODEL OF THE CANTILEVER ENGINE
CONFIG
%=====================================================
function X=freqres1(w,P)
%
%  X(1)= Delta V
%  X(2)= Delta Vdot
%  X(3)= Delta p
%  X(4)= Delta rhov
%  X(5)= Delta T
%  X(6)= (psi/pi*ro^2)*V
%  X(7)= Delta Tl
%
A1=zeros(7,7);B1=zeros(7,7); C1=zeros(7,1);
%=====================================================
% Row 1 Newtons Law for Diaphragm
A1(1,1)=1                                ;
% Row 2 Newtons Law for Diaphragm
A1(2,2)=(P.m+P.mb)/(pi*P.ro^2)^2         ;
% Row 3 Conservation of Mass
A1(3,1)=P.rhov                           ;
A1(3,3)=P.rhov*((pi*P.ri^2)^2)/P.sh      ;
A1(3,4)=P.Vo                             ;
% Row 4 Conservation of Energy
A1(4,4)=-(P.Vo*P.Po)/P.rhov              ;
A1(4,5)=P.rhov*P.Vo*P.cv                 ;
% Row 5 Ideal Gas
A1(5,3)=-1/(P.R*P.To)                    ;
A1(5,4)=1                                ;
A1(5,5)=P.Po/(P.R*P.To^2)                ;
% Row 6 Circuit for piezoelectric element
A1(6,1)=-1                               ;
A1(6,6)=P.Cob                            ;
% Row 7 Energy Conservation for liquid layer
A1(7,7)=P.CT                             ;
%=====================================================
% Row 1 Newtons Law for Diaphragm
B1(1,2)=1                                                          ;
% Row 2 Newtons Law for Diaphragm
B1(2,1)=-P.s/(pi*P.ro^2)^2                                         ;
B1(2,2)=-(P.b+P.bb)/(pi*P.ro^2)^2                                  ;
B1(2,3)=1                                                          ;
B1(2,6)=-1                                                         ;
% Row 3 Conservation of Mass
B1(3,3)=-P.betab*sqrt(P.M/(2*pi*P.Ru))*(1/sqrt(P.To))              ;
B1(3,5)=P.betab*sqrt(P.M/(2*pi*P.Ru))*((P.rhov*P.R)/(2*sqrt(P.To)));
B1(3,7)=P.B                                                        ;
% Row 4 Conservation of Energy
B1(4,5)=-P.hB                                                      ;
% Row 5 Ideal Gas
% B(:,5)=0
% Row 6 Circuit for piezoelectric element
B1(6,6)=-1/P.RLb
;
% Row 7 Energy Conservation for liquid layer
```

```
B1(7,3)=P.hfg*P.betab*sqrt(P.M/(2*pi*P.Ru))*(1/sqrt(P.To))              ;
B1(7,5)=-
P.hfg*P.betab*sqrt(P.M/(2*pi*P.Ru))*((P.rhov*P.R)/(2*sqrt(P.To)))       ;
B1(7,7)=-(P.hfg*P.B+P.U)                                                ;
%=====================================================
% Row 7 Energy Conservation for liquid layer
C1(7,1)=1                                                               ;
%SOLVING THE SYSTEM OF EQUATIONS USING COMPLEX NUMBER ANALYSIS.
X=(i*w*A1-B1)\C1                                                        ;
%=====================================================
```

```
%THIS FUNCTION CALCULATES THE SQUAR OF THE ERROR TO BE MINIMIZED
LATER/CANTILEVER ENGINE.
%============================
function K=squarederrorfcn(X,P1,M)
%M is the experimental data .
%P is the model parameter.
%X is the floating parameters in the model.
%============================
%P,M passed to the funcion form the lstsqrmthd file.
%Define the floating parameters.
P1.mb   =X(1);
P1.beta =X(2);
P1.U    =X(3);
P1.CT   =X(4);
P1.sh   =X(5);
P1.bb   =X(6);
P1.betab=P1.beta*P1.S                                              ;
P1.B    =P1.betab*sqrt(P1.M/(2*pi*P1.Ru))                          ;
P1.B    =P1.B*(10^(P1.Ah-(P1.Bh/(P1.To+P1.Ch))))/sqrt(P1.To)       ;
P1.B    =P1.B*( ((P1.Bh*log(10))/(P1.To+P1.Ch)^2)-(1/(2*P1.To)) );
%============================
f =M(:,1);% loading the first col in the data file ,f:frequency.
xm=M(:,2);% loading the 2nd  col in the data file ,DTF:Displacement
Transfer function.
xp=M(:,3);% loading the 3rd col in the data file ,DTFP: Displacement
Transfer function phase angle..
vm=M(:,4);% loading the 4th col in the data file ,VTF:Voltage Transfer
function..
vp=M(:,5);% loading the 5th col in the data file ,VTFP:Vltage Transfer
function Phase angle..
%============================
%Compute the predicted data from the model parameters
%============================
for j1=1:P1.Nfit
     warning off                    ;
     Y(:,j1)=freqres1(2*pi*f(j1),P1);
     warning on                     ;
end
%============================
Y1=(Y(1,:)/(pi*P1.ro^2))*1e6        ; %Y1 is the deflection in
micrometers
%============================
%Compute the square of the error for each data point ,sum it to the
%previuos error value and store it in J
%============================
K=0                                   ; %initialize the error to be
zero.
for i1=1:P1.Nfit
    K=K+((xm(i1)-abs(Y1(i1)))/xm(i1))^2;
end



%THIS PROGRAM IS TO IMPLEMENT THE LEAST SQURE METHOD IN MODEL
```

```
%FITTING/CANTILEVER ENGINE
%====================================
clear all ;
close all ;
clc       ;
%====================================
%Least square method
%====================================
EnginePars8mmCantilever ;
P1=P                    ;
%Calling the Specified MATLAB file (enginePars8mmCantilever)
%====================================
load testopencir.dat;
M=testopencir       ;
M=M(2:end,:)        ;
%========================================
%Define the floating parameters
%Initial guess for the floating parameters
%========================================
X0(1)=P1.mb*20         ;%THE EFFECTIVE MASS OF THE LIQUID
X0(2)=P1.beta          ;%EVAPORATION COFFICIENT
X0(3)=1000*P1.U        ;%HEAT LOSS COFFICIENT
X0(4)=P1.CT            ;%THERMAL INERTIA
X0(5)=P1.s*1.5         ;%HEATER STIFFNESS
X0(6)=P1.bb*1          ;%EFFECTIVE DAMPINF
%========================================
%set the conditions on each variable.
lb(1)=0;    ub(1)=1000        ;
lb(2)=0;    ub(2)=1           ;
lb(3)=0;    ub(3)=1000        ;
lb(4)=1e-9; ub(4)=1e-1        ;
lb(5)=0;    ub(5)=1000*P.s    ;
lb(6)=0;    ub(6)=1000*P.bb   ;
%========================================
%calling the Minimizer function to perform the optimization.
%========================================
P.Nfit=35                                                  ;%THE NUMBER OF
POINTS TO BE USED IN FITTING THE DATA
P1.Nfit=P.Nfit                                             ;
OPTIONS = OPTIMSET('MaxFunEvals ',5000,'MaxIter',1000)  ;
Xd = fmincon(@(X)
squarederrorfcn(X,P1,M),X0,[],[],[],[],lb,ub,[],OPTIONS)
Xd                                                         ;
%ASSIGNE THE OBTAINED PARAMETERS FROM THE OPTIMIZER TO THE FREE
PARAMETERS
P1.mb  =Xd(1)                                              ;
P1.beta=Xd(2)                                              ;
P1.U   =Xd(3)                                              ;
P1.CT  =Xd(4)                                              ;
P1.sh  =Xd(5)                                              ;
P1.bb  =Xd(6)                                              ;
%========================================
%LOADING THE MEASURED DATA
%========================================
f =M(:,1);
xm=M(:,2);
```

```
xp=M(:,3);% loading the 3rd col in the data file ,DTFP: Displacement
Transfer function phase spectrum
vm=M(:,4);% loading the 4th col in the data file ,VTF:Voltage Transfer
function
vp=M(:,5);% loading the 5th col in the data file ,VTFP:Vltage Transfer
function Phase spectrum
%=========================================
%UPDATE THE MODEL PARAMETERS WITH THE NEW VALUES OF THE FREE PARAMETERS
%=========================================
P1.betab=P1.beta*P1.S                                                    ;
P1.B=P1.betab*sqrt(P1.M/(2*pi*P1.Ru))                                    ;
P1.B=P1.B*(10^(P1.Ah-(P1.Bh/(P1.To+P1.Ch))))/sqrt(P1.To)                 ;
P1.B=P1.B*( ((P1.Bh*log(10))/(P1.To+P1.Ch)^2)-(1/(2*P1.To)) )            ;
P1.fn=(1/(2*pi))*sqrt(P1.s/(P1.m+P1.mb))                                 ;
P1.Cob=((pi*P1.ro^2)^2/P1.psi^2)*P1.Co                                   ;
P1.Rb=(P1.U/P1.hfg)/((P1.U/P1.hfg)+P1.B)                                 ;
P1.Rb=P1.Rb*(P1.betab/P1.rhov)*sqrt(P1.M/(2*pi*P1.Ru))*((P1.g+1)/(2*P1.g*
sqrt(P1.To)))                                                            ;
P1.Rb=1/P1.Rb                                                            ;
P1.Cb=(P1.Vo/(P1.g*P1.rhov*P1.R*P1.To))+(((pi*P1.ri^2)^2)/P1.sh)         ;
P1.fRbCb=(1/(2*pi))*(1/(P1.Rb*P1.Cb))                                    ;
P1.R1=(P1.b+P1.bb)/((pi*P1.ro^2)^2)                                      ;
P1.C1=((pi*P1.ro^2)^2)/P1.s                                              ;
P1.L1=(P1.m+P1.mb)/((pi*P1.ro^2)^2)                                      ;
P1.f1=P.Cb/(1+(P.Cb/P.C1))                                               ;
P1.f1=(1/(2*pi))*sqrt(1/(P1.f1*P1.L1))                                   ;
P1.fRbR=(P1.Rb)/((P1.b+P1.bb)/(pi*P1.ro^2)^2)                            ;
P1.CbC=(P1.Cb)/(((pi*P1.ro^2)^2)/P1.sh)                                  ;
%=============================================
%Calculate the DC calue of the transfer function
VolDC=((P1.Rb*P1.C1)/P1.U)*(P1.B/P1.rhov)                                ;
P1.XDC=VolDC/(pi*P1.ro^2)                                                ;
%Verify the calcualtions using the following realtionship
VolDC1=((P1.Rb*P1.C1)/P1.U)*(P1.betab*sqrt(P1.M/(2*pi*P1.Ru*P1.To))*(P1.h
fg/P1.To))                                                               ;
P1.XDC2=VolDC1/(pi*P1.ro^2)                                              ;
%Calcualting the transfer function value at frequency=P1.f1.
Xf1=(1/(pi*P1.ro^2))*(1/P1.U)*(P1.B/P1.rhov)                             ;
P1.Xf1=Xf1*(P1.L1/(1+(P1.Cb/P1.C1)))*(1/(P1.R1+P1.Rb*(P1.fRbCb/P1.f1)^2))
Xf2=(1/(pi*P1.ro^2))*(1/P1.U)*(P1.betab*sqrt(P1.M/(2*pi*P1.Ru*P1.To))*(P1
.hfg/P1.To))                                                             ;
P1.Xf2=Xf2*(P1.L1/(1+(P1.Cb/P1.C1)))*(1/(P1.R1+P1.Rb*(P1.fRbCb/P1.f1)^2))
%=============================================
for j1=1:P1.Nfit
     warning off                      ;
     Y(:,j1)=freqres1(2*pi*f(j1),P1) ;
     warning on                       ;
end
%=============================================
R=((Y(1,:)/(pi*P1.ro^2))*1e6)'        ;
R=abs(R)                              ;
Ph=angle(Y(1,:))'*(180/pi)            ;
%=============================================
subplot(2,1,1)
h1=loglog(f(1:P1.Nfit),abs((Y(1,:)/(pi*P1.ro^2))*1e6'),'g-'...
,f,xm,'bs',f(1:P1.Nfit),xm(1:P1.Nfit),'rs'        )
```

```
legend(h1,'Model \Gamma','Measured X_{k}/Q_{k}')
%
title([ 'mb=',num2str(P1.mb/P.mb),'mb'              ...
       ,'  beta=',num2str(P1.beta)                  ...
       ,'  U=',num2str(P1.U/(P1.hfg*P.B)),'*hfg*B' ...
       ,'  CT=',num2str(P1.CT)                      ...
       ,'  sh=',num2str(P1.sh/P.s),'s'              ...
       ,'  bb=',num2str(P1.bb/P.bb),'bb'            ...
       ,'  bb=',num2str(P1.bb)])
xlabel([ 'fn=',num2str(P1.fn)                       ...
       ,'  f1=',num2str(P1.f1)                      ...
       ,'  fRbCb=',num2str(P1.fRbCb)                ...
       ,'  Rb=',num2str(P1.Rb)                      ...
       ,'  Cb=',num2str(P1.Cb)                      ...
       ,'  R1=',num2str(P1.R1)                      ...
       ,'  C1=',num2str(P1.C1)                      ...
       ,'  U=' ,num2str(P1.U)                       ...
       ,'  mb=' ,num2str(P1.mb)])
%
subplot(2,1,2);
h2=semilogx(f(1:P1.Nfit),angle(Y(1,:))*(180/pi),'g-'     ...
                        ,f,xp,                  'bs' )     ...
legend(h2,'Model \Gamma','Measured X_{k}/Q_{k}')
xlabel(['Frequency (kHz)'])
ylabel(['Phase (deg)'])
grid on
% Vapor Pressure
figure
subplot(2,1,1); loglog(f(1:P1.Nfit),abs(Y(3,:)),'g-')...
title(['Vapor Pressure'])
xlabel(['Frequency (kHz)'])
ylabel(['Press (Pa/W)'])
grid on
subplot(2,1,2)
semilogx(f(1:P1.Nfit),angle(Y(3,:))*(180/pi),'g-' )
xlabel(['Frequency (kHz)'])
ylabel(['Phase (deg)'])
grid on
% Vapor Temperature
figure
subplot(2,1,1); loglog(f(1:P1.Nfit),abs(Y(5,:)),'g-' ) ...

title(['Vapor Temperature'])
xlabel(['Frequency (kHz)'])
ylabel(['Temp (K/W)'])
grid on
subplot(2,1,2); semilogx(f(1:P1.Nfit),angle(Y(5,:))*(180/pi),'g-' )   ...
xlabel(['Frequency (kHz)'])
ylabel(['Phase (deg)'])
grid on
% Voltage
Y(6,:)=Y(6,:)*((pi*P.ro^2)/P.psi)
figure
subplot(2,1,1); h3=loglog(f(1:P.Nfit),abs(Y(6,:)),'g-'  ...
                      ,f,vm,     'ks' )                  ...
                      legend(h3,'Model \Gamma','Measured X_{k}/Q_{k}')
title(['Voltage'])
```

```
xlabel(['Frequency (kHz)'])
ylabel(['Voltage (V)'])
grid on
subplot(2,1,2); h4=semilogx(f(1:P.Nfit),angle(Y(6,:))*(180/pi),'g-'   ...
                        ,f,vp                                ,'bs' )    ...
                        legend(h4,'Model \Gamma','Measured X_{k}/Q_{k}')
xlabel(['Frequency (kHz)'])
ylabel(['Phase (deg)'])
grid on
%Save the plots in txt file.
data=[f,xm,xp]
save expreults.dat  data -ascii
data=[R,Ph]
save fitresults.dat data -ascii
```

APPENDIX D

MATLAB CODE FOR LEAST SQUARE METHOD (ENCLOSED ENGINE CONFIGURATION)

```
%%THIS FILE STORES THE DEFAULT PARAMETERS OF THE ECLOSE ENGINE,INCLUDING
%PF5060 WROKING FLUID PROPETIES
clear all;
close all;
clc      ;
% Default parameters
%=======================================
% Properties of the fluid
%=======================================
P.rhov=3.53                              ;
P.rhol=1775                              ;
P.mul=467.04e-6                          ;
P.M=338/1000                             ;
P.Ru=8.31                                ;
P.Ah=9.73                                ;
P.Bh=1562                                ;
P.Ch=0                                   ;
P.cp=755.2                               ;
Psat=25.097                              ;
P.R=(Psat*1000)/(P.rhov*(273+21))        ;
P.cv=P.cp-P.R                            ;
P.g=P.cp/P.cv                            ;
P.hfg=94.05e03                           ;
%====================================
% Properties of the engine
%====================================
P.s    =1485             ;
P.ro   =(5e-3)/2         ;
P.ri   =P.ro             ;
P.L    =75e-6            ;
P.S    =pi*P.ri^2        ;
P.Vo   =P.S*P.L          ;
P.beta=0.0003            ;
P.betab=P.beta*P.S       ;
P.sh   =1740             ;
P.b    =1.0              ;

%====================================
%  Environmental parameters
%====================================
P.To=294                           ;
P.Po=10^(P.Ah-(P.Bh/(P.To+P.Ch)));
%====================================
```

```
%  Computed parameters
%====================================
P.B=P.betab*sqrt(P.M/(2*pi*P.Ru))                                                ;
P.B=P.B*(10^(P.Ah-(P.Bh/(P.To+P.Ch))))/sqrt(P.To)                                ;
P.B=P.B*( ((P.Bh*log(10))/(P.To+P.Ch)^2)-(1/(2*P.To)) )                          ;
P.U=1*P.B*P.hfg                                                                  ;
P.Rb=(P.U/P.hfg)/((P.U/P.hfg)+P.B)                                               ;
P.Rb=P.Rb*(P.betab/P.rhov)*sqrt(P.M/(2*pi*P.Ru))*(P.g+1)/(2*P.g*sqrt(P.To
))
P.Rb=1/P.Rb                                                                       ;
P.R1=((P.b)/((pi*P.ro^2)^2))                                                      ;
P.Cb=(P.Vo/(P.g*P.rhov*P.R*P.To))+(((pi*P.ri^2)^2)/P.sh)                          ;
P.C1=((pi*P.ro^2)^2)/P.s                                                          ;
P.fRbCb=(1/(2*pi))*(1/(P.Rb*(P.Cb+P.C1)))                                         ;
P.Ib=((P.U/(P.hfg*P.B))+1)                                                        ;
P.Ib=((P.Ib)*(P.rhov*P.hfg))                                                      ;
P.Ib=1/(P.Ib)                                                                     ;
```

```
%THIS SUBROTUINE IS USED TO CONSTRUCT THE MODEL OF THE CANTILEVER ENGINE
CONFIG
function X=freqres1(w,P1)
%=====================================================
Z=(1./(P1.Rb*P1.C1))-(P1.R1*P1.Cb*(w.^2))         ;
Z=Z+(((P1.R1./P1.Rb)+(P1.Cb./P1.C1)+1)*(i*w))     ;
Z=(1./Z)                                          ;
X=(P1.Ib)*(Z)                                     ;
%=====================================================
```

```
%THIS FUNCTION CALCULATES THE SQUAR OF THE ERROR TO BE MINIMIZED
LATER/ENCLOSED ENGINE.
%============================
function K=squarederrorfcn(X,P1,M)
%M is the experimental data .
%P is the model parameter.
%X is the floating parameters in the model.
%============================
%P,M passed to the funcion form the lstsqrmthd file.
%Define the floating parameters.
P1.beta =X(1);
P1.U    =X(2);
P1.b    =X(3);
%
P1.betab  =P1.beta*P1.S                                                    ;
P1.B      =P1.betab*sqrt(P1.M/(2*pi*P1.Ru))                                ;
P1.B      =P1.B*(10^(P1.Ah-(P1.Bh/(P1.To+P1.Ch))))/sqrt(P1.To)             ;
P1.B      =P1.B*( ((P1.Bh*log(10))/(P1.To+P1.Ch)^2)-(1/(2*P1.To)) )        ;
%
P1.Ib     =((P1.U/(P1.hfg*P1.B))+1)          ;
P1.Ib     =((P1.Ib)*(P1.rhov*P1.hfg))        ;
P1.Ib     =1/(P1.Ib)                         ;
%
P1.Cb     =(P1.Vo/(P1.g*P1.rhov*P1.R*P1.To))+(((pi*P1.ri^2)^2)/P1.sh)       ;
P1.Rb     =(P1.U/P1.hfg)/((P1.U/P1.hfg)+P1.B)                              ;
P1.Rb=P1.Rb*(P1.betab/P1.rhov)*sqrt(P1.M/(2*pi*P1.Ru))                      ;
*(P1.g+1)/(2*P1.g*sqrt(P1.To))                                             ;
P1.Rb     =1/P1.Rb                                                         ;
%
P1.fRbCb  =(1/(2*pi))*(1/(P1.Rb*(P1.Cb+P1.C1)))                            ;
%
P1.R1     =(P1.b)/((pi*P1.ro^2)^2)                                         ;
%============================
f =M(:,1); % loading the first col in the data file ,f:frequency.
xm=M(:,2);% loading the 2nd  col in the data file ,DTF:Displacement
Transfer function.
xm=xm'   ;
xp=M(:,3);% loading the 3rd col in the data file ,DTFP: Displacement
Transfer function phase angle..
%============================
%Compute the predicted data from the model parameters
%============================
for j1=1:P1.Nfit
     warning off                    ;
     Y(:,j1)=freqres1(2*pi*f(j1),P1);
     warning on                     ;
end
Y1=(Y(1,:)/(pi*P1.ro^2))*1e6        ;
%============================
%Compute the square of the error for each data point ,sum it to the
%previuos error value and store it in J
%============================
K=0; %initialize the error to be zero.
for i1=1:P1.Nfit
    K=K+((xm(i1)-abs(Y1(i1)))/xm(i1))^2;
end
%THIS PROGRAM IS TO IMPLEMENT THE LEAST SQURE METHOD IN MODEL
```

```
%FITTING/ENCLOSED ENGINE CONFIG
clear all;
close all;
clc
%Engine specifications :
%5 mm Heater ,5 mm SiNx membrane.
%95% vapor
%75mic thick
%Rh=13.0 ohm
%FC5060
%data collected on 06/27/07 for 1Hz and 10Hz 1% duty cyc
%This programme is modified to consider the damping effect(R in th
electrical
%circut analogy) not to be zero.
%====================================
%Least square method
%====================================
EnginePars8mmCantilever;
P1=P                    ;
%Calling the Specified MATLAB file (enginePars8mmCantilever)
%====================================
load testopencir.dat;
M=testopencir       ;
M=M(2:end,:)        ;
%========================================
%Define the floating parameters;
%Initial guess for the floating parameters;
%========================================
X0(1)=P1.beta*1    ;          %floating parameter.
X0(2)=P1.U*30      ;
X0(3)=P1.b*1       ;
%set the conditions on each variable.
lb(1)=1e-5      ;       ub(1)=1         ;
lb(2)=1e-9      ;       ub(2)=1000      ;
lb(3)=1e-9      ;       ub(3)=100*P.b   ;
%========================================
%calling the Minimizer function to perform the optimization.
%========================================
%OPTIONS(1)=1;
P.Nfit  =35
P1.Nfit =P.Nfit
OPTIONS = OPTIMSET('MaxFunEvals ',5000,'MaxIter',1000)
Xd      = fmincon(@(X)
squarederrorfcn(X,P1,M),X0,[],[],[],[],lb,ub,[],OPTIONS)   ;
Xd
%
P1.beta  =Xd(1);
P1.U     =Xd(2);
P1.b     =Xd(3);
%
P1.betab =P1.beta*P1.S                                          ;
%
P1.B     =P1.betab*sqrt(P1.M/(2*pi*P1.Ru))                      ;
P1.B     =P1.B*(10^(P1.Ah-(P1.Bh/(P1.To+P1.Ch))))/sqrt(P1.To)     ;
P1.B     =P1.B*( ((P1.Bh*log(10))/(P1.To+P1.Ch)^2)-(1/(2*P1.To)) );
%
P1.Ib    =((P1.U/(P1.hfg*P1.B))+1)  ;
```

```
P1.Ib    =((P1.Ib)*(P1.rhov*P1.hfg));
P1.Ib    =1/(P1.Ib)                  ;
P1.Cb=(P1.Vo/(P1.g*P1.rhov*P1.R*P1.To))+(((pi*P1.ri^2)^2)/P1.sh)        ;
P1.Rb   =(P1.U/P1.hfg)/((P1.U/P1.hfg)+P1.B)                            ;
P1.Rb   =P1.Rb*(P1.betab/P1.rhov)*sqrt(P1.M/(2*pi*P1.Ru))
*(P1.g+1)/(2*P1.g*sqrt(P1.To))                                         ;
P1.Rb   =1/P1.Rb                                                       ;
%
P1.C1=((pi*P1.ro^2)^2)/P1.s                                            ;
P1.R1=(P1.b)/((pi*P1.ro^2)^2)                                          ;
%
P1.fRbCb=(1/(2*pi))*(1/(P1.Rb*(P1.Cb+P1.C1)))                          ;
%=======================================
f  =M(:,1);
xm =M(:,2);
xp =M(:,3);
%
P1.Rb=(P1.U/P1.hfg)/((P1.U/P1.hfg)+P1.B)                              ;
P1.Rb=P1.Rb*(P1.betab/P1.rhov)*sqrt(P1.M/(2*pi*P1.Ru))*((P1.g+1)/(2*P1.g*
sqrt(P1.To)));
P1.Rb=1/P1.Rb                                                         ;
P1.Cb=(P1.Vo/(P1.g*P1.rhov*P1.R*P1.To))+(((pi*P1.ri^2)^2)/P1.sh)      ;
P1.fRbCb=(1/(2*pi))*(1/(P1.Rb*(P1.Cb+P1.C1)))                         ;
P1.C1=((pi*P1.ro^2)^2)/P1.s                                           ;
P1.CbC=(P1.Cb)/(((pi*P1.ro^2)^2)/P1.sh)                               ;
%
%=====================================
for j1=1:P1.Nfit
     warning off                  ;
     Y(:,j1)=freqres1(2*pi*f(j1),P1);
     warning on                   ;
end
%=====================================
R=((Y(1,:)/(pi*P1.ro^2))*1e6)';
R=abs(R)                     ;
Ph=angle(Y(1,:))*(180/pi)    ;
%=====================================
figure
subplot(2,1,1)
h1=loglog(f(1:P1.Nfit),abs((Y(1,:)/(pi*P1.ro^2))*1e6'),'g-'  ...
                  ,f,xm,'bs')
ylabel('Disp amp(μm/w)')
%
title([ '  beta=',num2str(P1.beta)                  ...
       ,'  U =',num2str(P1.U/(P1.hfg*P1.B)),'*hfg*B' ...
       ,'  sh=',num2str(P1.sh/P1.s),'s'])

xlabel(['  Rb =',num2str(P1.Rb)                    ...
       ,'  C1 =',num2str(P1.C1)                    ...
       ,'  U  =',num2str(P1.U )                    ...
       ,'  b =' ,num2str(P1.b )                    ...
       ,'  fRbCb=',num2str(P1.fRbCb) ])
legend(h1,'Model \Gamma','Measured X_{k}/Q_{k}')
grid on
subplot(2,1,2)
semilogx(f(1:P1.Nfit),Ph ,'g-'  ...
                       ,f,xp ,'bs' )
```

```
xlabel(['Frequency (kHz)'])
ylabel(['Phase (deg)'])
title('Phase of the dispalcment tranfer function')
 grid on
 figure
 subplot(2,1,1)
h2=loglog(f(1:P1.Nfit),abs((2*pi*f(1:P1.Nfit)').*(Y(1,:)/(pi*P1.ro^2))*1e
6')*1e-3,'g-'...
,f,abs((2*pi*f).*xm)*1e-3,'bs')
legend(h2,'Model \Gamma','Measured X_{k}/Q_{k}')
ylabel(' \Gamma[kfp] (mm/s/W)')
title('Velocity transfer function ')
grid on
%=================================================================
```